POLITECNICO DI TORINO
Repository ISTITUZIONALE

Experimental validation of Orcaflex-based numerical models for the PEWEC device

(Article begins on next page)

15 May 2024

Check for updates

Experimental validation of Orcaflex-based numerical models for the PEWEC device

F. Niosi [a,*], E. Begovic [b], C. Bertorello [b], B. Rinauro [b], G. Sannino [c], M. Bonfanti [a], S.A. Sirigu [a]

[a] *Politecnico di Torino, Department of Mechanical and Aerospace Engineering, Italy*
[b] *University of Naples Federico II, Department of Industrial Engineering, Italy*
[c] *ENEA Division "Models and Technologies for Disaster Risks Reduction", Italy*

ABSTRACT

To design a Wave Energy Converter mooring system that ensures maintainability, resistance, and low costs, without affecting productivity, it is necessary to foster reliable numerical models. In the present paper, the validation of Orcaflex© simulations against the experiment results of the Pendulum Wave Energy Converter (PEWEC) 1:25 scale model, conducted at the University of Naples Federico II, is presented. The experiments consist of free-decay and static pull-out tests to assess the inertial properties of the model and mooring system; tests in operative and extreme regular and irregular waves to fully characterize the mooring system and the device dynamics. The same wave records measured in the towing tank have been used in numerical simulations. PEWEC motion results from numerical simulations and experiments are given in terms of Response Amplitude Operators (RAOs) for regular waves, as statistical values in tabular form, and in Taylor's diagrams for irregular waves. The most probable fairleads tensions for the load dimensioning have been obtained from the Generalized Extreme Value (GEV) distribution of experimental and numerical data. The obtained differences show that the numerical model accurately predicts the experimental data and correctly estimates the dimensioning load of the mooring lines.

1. Introduction

The climate crisis characterizing the last few decades and the difficulty in finding energy sources, due to delicate geopolitical situations, make renewable energies an essential source for the near future. Among these, wave energy plays a fundamental part in the energy scenario and there are more than one thousand Wave Energy Converters (WECs) prototypes nowadays, as reported in Xu and Wang (2019).. A very detailed overview of the research projects in the world, touching upon development history, working principles, main dimensions and sea sites, and possible mooring systems can be found in Clemente et al. (2021), Qiao et al. (2019), Fenu et al. (2020) and Golbaza et al. (2022). A comprehensive review of the WEC research using Computational Fluid Dynamics (CFD) over the past two decades is reported in Windt et al. (2020), clearly indicating the importance of acquiring reliable numerical tools for WEC research and development, as it gives the possibility to simulate various environmental and physical conditions without significant restrictions compared to experiments.

In the design of a Wave Energy Converter, the first step is the analysis

of the wave resource relating to the installation site, which must be carefully chosen. For the given installation site, the device must be designed to maximize its production. And finally, the mooring system must be designed to withstand and ensure the safety of the device during a storm.

To date, the world standard perspective lacks a clear description of the criteria and standards that the WEC must comply with to be defined as adequate. A set of recommendations targeting WEC mooring guidelines and standards has been published as a deliverable of EU project OPERA (Khalid et al., 2019). A review and suggestions for suitable mooring design, according to the WEC dimensions and working principles, are given in Xu and Wang. (2019). The authors highlighted that the elastic synthetic rope has great potential in the application of WEC mooring system and that the hybrid mooring system could be a good solution for the WEC station-keeping problem. Barrera et al. (2019) conducted an experimental study to examine the dynamic characteristics of mooring lines and evaluated how the damping effect varied under different motion conditions. The authors pointed out the importance of proper upscaling to correctly withdraw the results from experiments.

The importance of the pre-tension and the choice of both mooring material and geometry in determining the stiffness characteristics of a mooring system for a floating WEC was studied by Johanning et al. (2006). They concluded that a good understanding of the related stiffness and motion characteristics is essential to develop suitable design guidance that would address not only the issue of line failure but also satisfy the requirement for high-energy conversion efficiency.

Cerveira et al. (2013) conducted a numerical assessment of the impact of the mooring system on the effectiveness of the WEC, specifically in terms of surge and heave motions and absorbed power. The authors highlighted that the actual mooring catenary chain lines have a minimal effect on the dynamics of floating wave energy converters and the amount of captured wave energy.

Gubesch et al. (2022) performed a systematic experimental investigation into the effects of different mooring configurations on the hydrodynamic performance of a 1:36 scaled Oscillating Water Column (OWC) Wave Energy Converter model. Enhanafi et al. (2017) investigated the intact and damaged survivability of a floating–moored OWC device using physical model experiments and CFD simulations. Different extreme wave conditions have been tested using irregular and regular waves and authors highlighted the importance of investigating survival conditions with a damaged mooring system instead of simply using the same conditions derived for the intact mooring system. Paduano et al. (2020) tested and compared three models: an in-house QS solver, a commercial industry-standard software (OrcaFlex©), and an open-source software (MoorDyn). Validation of the models has been done by experimental data and was found that the Quasi-Static model and OrcaFlex© show good agreement.

The mooring systems used for WECs must satisfy two counteracting objectives: ensuring resistance during extreme events and minimizing their impact on the WEC's productivity. This creates a trade-off because to avoid influencing the hull dynamics, it is preferable to use light and thin mooring lines rather than thick and heavy ones that can guarantee resistance. Consequently, designing the mooring system for a WEC becomes a critical and intricate phase, both in terms of cost and safety. Achieving an efficient and cost-effective mooring system requires multiple iterations using reliable numerical models that can evaluate the mooring characteristics within reasonable time frames.

The present research focuses on the validation of the numerical simulations performed by Orcaflex© through experimental tests carried out at the towing tank of the University of Naples Federico II. The experiments on the 1:25 model scale of the PEWEC prototype and its specifically designed mooring layout have been performed in operative and extreme regular and irregular waves to fully characterize the mooring system and the PEWEC dynamics.

A detailed description of the device and its mooring system is given in Section 3. The numerical modeling is explained in Section 4 and the experiment is described in Section 5. For all tested conditions, results are reported and compared for surge, pitch, and roll motions and tensions in mooring lines. For operative waves, a GEV distribution has been created to determine the most probable maxima for load dimensioning.

2. The PEWEC technology

The PEWEC concept was born from the collaboration between Ente per le Nuove tecnologie, l'Energia e l'Ambiente (ENEA), and the Politecnico di Torino within the "MISE-ENEA Program Agreement" funding aimed at the development of a renewable and clean technology that can be used for the sustenance of small energy communities disconnected from the national electricity grid, such as small islands. At present, the technology stands at a Technology Readiness Level (TRL) between 4 and 5. In 2015, a series of experiments were carried out on a 1:12 scale prototype at the CNR INSEAN towing tank in Rome with the aim to validate the numerical model of the working principle of the pendulum for predicting the power generated by the device as depicted in Pozzi et al. (2018a) and Pozzi et al. (2018b). Concerning the device power

production, PEWEC can be considered as a floating mass exposed to wave excitations. As shown in Fig. 1 and deepened in Bonfanti and Giorgi (2022) and Bonfanti and Sirigu (2023), the hull is linked to a pendulum by means of a power take-off (PTO), used to extract power from the sea waves, which is the system's main purpose.

The power extraction performance is directly linked to the pitch motion of the floater (Sirigu et al., 2018), and therefore PEWEC mooring system design should not affect the pitching motion in operational conditions. The numerical models relating to the hull, pendulum, and power take-off optimized subsystems were validated (Pozzi et al. 2017a, Pozzi et al. 2017b). Each of the three subsystems was optimized through a genetic algorithm as detailed in Sirigu et al. (2020). To achieve a TRL 6–7, open sea trial, it is necessary to guarantee the safety of the device at sea. Therefore, within the project "MISE-ENEA PROGRAM AGREEMENT 2019–2021″ the feasibility of a full-scale system was evaluated considering the island of Pantelleria as a case study. The project focused on the design of the mooring system, a critical component in terms of system survival and costs. The mooring system for WECs must meet the following basic requirements:

- Ensure proper seaworthiness of the vessel.
- Guarantee the survival of the system in extreme events in accordance with the current legislation.
- Have a low impact on the dynamics and therefore on the performance of electricity production in operational wave conditions.
- Have a low cost.

The characteristics of the PEWEC device are reported in Table 1, a render of the hull device is shown in Fig. 2, and a render of the Pendulum and the Power Take Off system of the device is presented in Fig. 3.

The mooring system considered in this work is shown in Fig. 3. It consists of 4 lines of catenaries, 4 drag anchors, 4 jumpers, and 9 clump weights lying on the seabed for each mooring line. The description of the mooring system is further detailed in Section 3.1.

Prior to the design of a full-scale prototype, it is necessary to validate the numerical models adopted for the design and simulation of the mooring system. In the presented work, the numerical simulations by
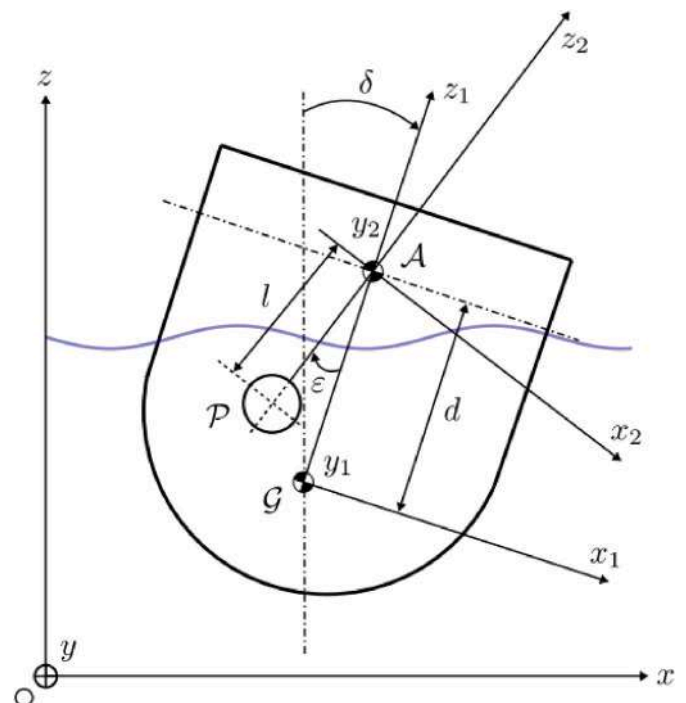

Fig. 1. Scheme of PEWEC device.

Table 1
PEWEC main characteristics.

Parameter	Symbol	Full-scale Value	SI Unit
Length	L	14.8	(m)
Width	B	22.5	(m)
Height	D	7.4	(m)
Draft	T	4.81	(m)
Vertical position of CG (from deck)	VCG	−3.622	(m)
Mass	M	1118000	(kg)
Moment of inertia around x-axis	I_{44}	55354173	(kgm^2)
Moment of inertia around y-axis	I_{55}	29978075	(kgm^2)
Moment of inertia around z axis	I_{66}	72150648	(kgm^2)

OrcaFlex© have been validated against a series of experiments carried out on a 1:25 scale model of the PEWEC device in the towing tank of the University of Naples Federico II.

3. Model description

The Pendulum Wave Energy Converter (PEWEC) CAD design and the built model are shown in Fig. 4. The scale of 1:25 has been chosen as the compromise between the mooring system configuration, the wave maker working range and the towing tank dimensions. By using the Froude number to scale the model, it becomes possible to replicate the potential flow theory forces and the main actions exerted by the mooring on the device. The internal design allows an easy modification of the longitudinal and vertical positions of the ballast weights, to achieve the scaled inertia and mass characteristics. The ballasts consist of steel blocks of different sizes, equipped with slots that allow them to be screwed onto the Rexroth bars.

The final values of the PEWEC inertial properties were measured by an inertial balance shown in Fig. 5. The accelerometer positioned in the center of upper arm measures at the sampling frequency of 1000 Hz. The PEWEC model is connected by bands to the aluminum structure, free to swing around the roll and pitch axes. The first step is the measurement of the vertical coordinate of the center of gravity, using a procedure similar to the standard ship inclining test. The second phase is the measurement of the periods of roll and pitch oscillations to determine the radii of gyration. These tests were repeated three times and around 100 oscillations have been analyzed to calculate the mean period of the roll and pitch motions.

Table 2 presents and compares the scaled and measured values. The 1.1% difference in weight can be attributed to the measurement instrumentation, installed on board of the model, and therefore was considered acceptable. All other measured values consequently have been upscaled and used in the numerical model Orcaflex© for the validation of the numerical simulations.

3.1. Mooring system

The coupling between the mooring system and the vessel plays a fundamental role in the energy production obtained from the pendulum motion. The design of the mooring system is based on two main ideas:

- Extreme Event Resistance: the design of each component (chain, polyester lines, swivels, buoys, etc.) is obtained by considering extreme event conditions according to the installation site as detailed in Det Norske Veritas. (2014).
- No impact during operative conditions: the mooring system for a WEC should also be designed to avoid pitch losses during the operative condition when sea states are not harsh.

Due to the challenges of meeting all the previous requirements simultaneously, an iterative approach has been adopted for the mooring design. The mooring system undergoes numerical simulations to verify its ability to withstand extreme events. Then an analysis of its impact on energy production can be conducted, as outlined in Niosi et al. (2021). If the results are unsatisfactory, it is necessary to modify the system design. The mooring system used for the experimental and numerical testing, shown in Fig. 6, is the final design that satisfies the previously indicated requirements.

The sea depth h = 1.28m, shown in Fig. 6, is calculated by scaling the depth of the site of installation. Scaling operations are fundamental for the mooring characterization. The main components of the mooring system are shown in Fig. 6 and their characteristics are reported in Table 3 for both the prototype and the scaled model tested in the towing tank. All the mooring properties have been determined from the full-scale values following the Froude scaling procedure. It is worth noticing that since the selected mooring system is a catenary mooring system, the mass properties of the lines have been scaled down. A spring was added to scale down the mooring stiffness: considering the chain and spring as springs in series, the chain stiffness can be neglected because it is three orders of magnitude larger. To design the 1:25 model, the full-scale prototype was scaled down using the Froude scaling procedure detailed by Barltrop (1998). As the mooring system is a catenary

Fig. 3. PEWEC Mooring system 1:25 scaled model.

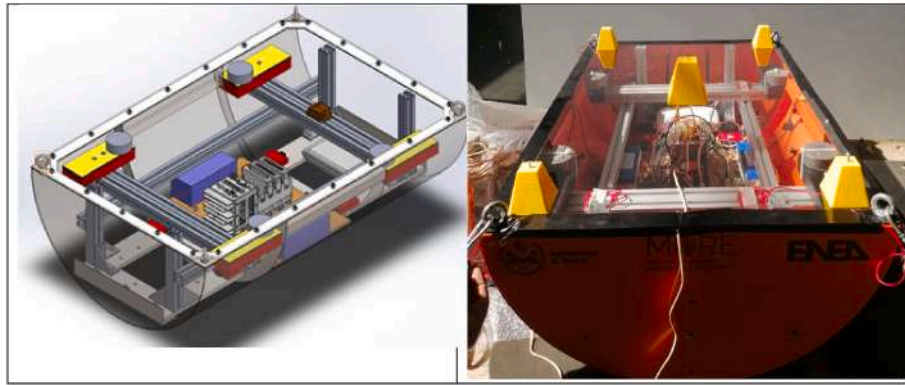**Fig. 2.** Render of the PEWEC hull, the Pendulum and the PTO.

Fig. 4. Cad and prototype of the PEWEC device.

type, its most important feature is the mass term. Therefore, the linear mass properties were scaled down according to the scale factors reported in Table 3. Additionally, a spring was included where numerical simulations suggested that the chain may become taut (snap events), as the mass term scales with the square of the scaling factor and the EA of the chains with the cube. The spring chosen had a different diameter, as it was selected from catalog to have the stiffness characteristics of the full-scale chain but scaled down for the smaller model. The spring characteristics have been calculated following equation (1).

$$\frac{1}{K_{spring}} = \frac{1}{K_{scaled}} - \frac{1}{K_{chain}} = \frac{L_{fullscale}}{(EA)_{fullscale}}\lambda^2 - \frac{4(L_{fullscale} - L_{spring})}{E_{chain}\pi(d_{chain})^2} \cong \frac{L_{fullscale}}{(EA)_{fullscale}}\lambda^2$$
$$- \frac{L_{chain}}{(EA)_{chain}}$$

$$(1)$$

In equation (1), (K_{scaled}) is the total stiffness of the system, (K_{chain}) the chain stiffness, and (K_{spring}) the stiffness of the spring. The equation can be approximated by using the full-scale stiffness of the mooring line $(L_{fullscale})$, divided by the EA (Young's modulus multiplied by cross-sectional area) of the full-scale line ignoring the effect of the chain's

diameter. The simplified equation becomes $\frac{L_{fullscale}}{(EA)_{fullscale}}\lambda^2$, where lambda is the scaling factor, and (L_{chain}) is the length of the chain.

In equation (1) the chain axial stiffness is calculated according to the semi-empirical formulation suggested in equation (2):

$$(EA)_{chain} = 0.854 \bullet 10^8 d^2 \ (kN) \quad studless \ chain \qquad (2)$$

It is important to note that the spring was exclusively included in the reduced-scale model to ensure that not only the mass of the mooring but also the stiffness of the line was proportionately scaled.

Table 3 shows the values of the variables in the full-scale system and

Table 2
Design Vs experimental values.

Parameter	SI Unit	Scaled Value	Exp. Measure	Difference (%)
M	(kg)	71.552	72.360	1.1
T	(m)	0.192	0.196	2.0
VCG	(m)	−0.145	−0.139	4.1
I_{44}	(kgm^2)	5.668	5.827	2.8
I_{55}	(kgm^2)	3.070	3.334	8.6
I_{66}	(kgm^2)	7.388	7.388	0

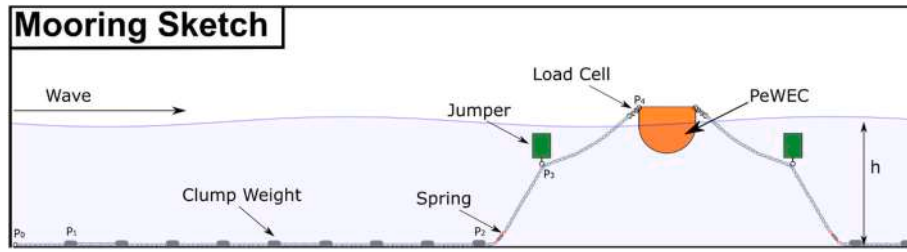**Fig. 5.** PEWEC on inertial balance.

Fig. 6. Mooring layout.

Table 3
Mooring system description: model-scale and full-scale properties.

Chain Description	Model-scale	Full-scale	SI Unit	Scale Factor
Mass per unit length	0.651	406.9	(kg/m)	λ^2
Outer diameter	0.0057	0.193	(m)	λ
EA (Axial Stiffness)	N/D	43.34e6	(kN)	λ^3
Jumper Description				
Mass	0.512	8000	(kg)	λ^3
Volume	0.0016	25	(m³)	λ^3
Height	0.184	4.6	(m)	λ
Clump Weights				
Mass	0.672	10500	(kg)	λ^3
Volume	1.1e-04	1.75	(m³)	λ^3
Height	0.02	0.5	(m)	λ

their corresponding scaled values according to the Froude scaling ($\lambda = 25$). Table 4 lists the characteristics of the additional components in the scale model, i.e. the spring that scales the stiffness of the individual catenary line and the load cell at the fairlead.

4. Device modeling via Orcaflex©

The PEWEC device was modeled numerically using Orcaflex© to compare the simulations against the experimental data and to improve the design, especially for what concerns the mooring system. Orcaflex© computes the device dynamics in waves by numerically solving the time domain equation of motions accounting for both first-order and second-order effects. In this study, OrcaWave© was utilized to calculate the hydrodynamic coefficients, including added mass and damping coefficients, excitation forces, and second-order forces which were then incorporated into the time domain simulations using Orcaflex© (Orcina, 2020). Second-order hydrodynamic forces have been computed by using Newman's approximation instead of solving the full QTF problem (Newman, 2017). A mesh sensitivity analysis was performed to set the element size to obtain accurate hydrodynamic results in Orcawave as detailed in Niosi et al. (2022).

The frequency domain equation of motion of the device can be written as follow:

$$\left[-i\,\omega^2([M]+[A(\omega)]) + i\omega([B_{rad}(\omega)]+[B_{vislin}]) + [K] \right]\{\eta\} = \{F_{w(1st)}(\omega)\} + \{F_{w(2nd)}(\omega^2)\} + \{F_{moor}\}$$

(3)

in which:

- ω is the wave frequency.
- $[M]$ is the mass matrix of the device and $[A(\omega)]$ is its frequency-dependent added mass matrix computed through OrcaWave BEM software.
- $[B_{rad}(\omega)]$ is the device frequency-dependent radiation damping matrix computed through OrcaWave.
- $[B_{vlin}]$ is the 6 × 6 linearized viscous damping matrix and in the following analyses only the terms in positions (4,4)-Roll and (5,5)-Pitch are non-zeros.

- $[K]$ is the hydrostatic stiffness matrix of the device.
- $\{F_{w(1st)}(\omega)\}$, $\{F_{w(2nd)}(\omega^2)\}$, $\{F_{moor}\}$ are the external force vectors. Respecevely first order wave load, second order wave loads and mooring forces acting on the device.

The equation of motion is transformed from frequency to time domain following Cummins (1962):

$$(m+m_\infty)\,\ddot{\eta}(t) + \int_{-\infty}^{t} h_r(\tau)\dot{\eta}(t-\tau)d\tau + h_k\eta(t) = f_e(t)$$

(4)

While the hydrostatic term h_k can be easily determined based on the submerged geometry, the remaining coefficients must be calculated by directly integrating the potential flow. Ogilvie (1964) found a simpler way to overcome this issue by defining the Fourier-domain equivalents of these terms as:

$$Ar(\omega) = m_\infty - \frac{1}{\omega}\int_{R+} h_r(\tau)\sin(\omega t)d\tau$$

(5)

$$Br(\omega) = \frac{1}{\omega}\int_{R+} h_r(\tau)\cos(\omega t)d\tau$$

(6)

where {Ar, Br} are the frequency-dependent added mass and radiation damping, respectively. These equations, known as Ogilvie's relation, show that:

$$\lim_{\omega_i \to \infty} Ar(\omega_i) = m_\infty$$

(7)

where m_∞ is the infinite frequency added mass. The equation's parameters are computed using the boundary element method (BEM-Orcawave) software, which solves the boundary problem numerically. Note that equation (7) implies the stability of the convolution term which is solved numerically by Orcaflex© during time-domain computation.

Concerning the mooring system, Orcaflex© solves the analytic catenary equation which accounts for simple properties of a line, such as weight, buoyancy, and axial stiffness. The top, side, frontal and isometric view setup are reported in Fig. 7 and further explanation of the model setup can be found in Niosi et al. (2021).

In equation (4), $f_e(t)$ accounts for the contribution of the mooring action applied to the body. OrcaFlex© imports the hydrodynamical properties of the device, as evaluated by a BEM, and resolves Cummins equation by computing the impulse response function of the radiation force. Although OrcaFlex© can be used for frequency-domain analysis,

Table 4
Model scale spring and load cells characteristics.

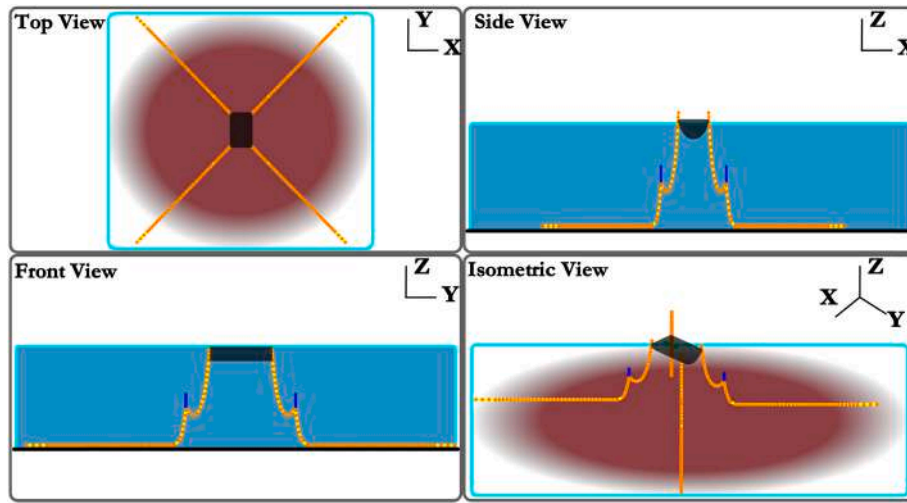| Load Cell Description		
Mass per unit length	0.173	(kg/m)
Outer diameter	0.0015	(m)
EA (Axial Stiffness)	N/D	(kN)
Spring Description		
Mass per unit length	1.32	(kg/m)
Outer diameter	0.0075	(m)
Stiffness (N/mm)	25.33	(kN/m)
Length	0.1	(m)

Fig. 7. Orcaflex© numerical model, top view, side view, front view and isometric view.

its primary purpose is for nonlinear mooring dynamics, so it is not considered here. The mooring system in the case of wave energy is well-represented by a dynamic solver, which OrcaFlex© accomplishes through a lumped-mass approach. The dynamic equation for the k-th node in a lumped-mass approach is given by:

$$(\widehat{m}_k + \widehat{a}_k) \cdot \ddot{\widehat{r}}_k = \widehat{f}_{EA,k-} + \widehat{f}_{EA,k+} + \widehat{f}_{C,k-} + \widehat{f}_{C,k+} + \widehat{f}_{B,k} + \widehat{f}_{Dn,k} + \widehat{f}_{Da,k} + \widehat{f}_{ext,k}$$

(8)

where $\{mk, ak\}$ are the mass and added mass of the k-th node, respectively, and r_k is the position of the k-th node relative to a global fixed frame of reference O_{x1x2x3} located on the waterline; $\{f_{EA}, f_C\}$ are the axial stiffness and damping force, respectively, due to the line section properties. The forces caused by the interaction between the nodes k and k+1 and k and k−1 are expressed by subscripts k+ and k−, respectively. The node net buoyancy force is expressed by $\widehat{f}_{B,k}$, and $\{\widehat{f}_{Dn,k}, \widehat{f}_{Da,k}\}$ represent the drag normal and axial force, respectively, caused by the velocity of the k-th node in the fluid. $\widehat{f}_{ext,k}$ represents the external actions such as the interaction of the node with the seabed or the forces applied to the node by line attachments (e.g., buoy or clump-weights), among others.

The use of a BEM is typically required to evaluate the response of a body in water, but Morison equation (Morison et al., 1950) can be used for a slender body, enabling the use of the added mass and drag coefficients instead of a BEM. By solving equation (8), it is possible to determine the total load on the last node, which is directly connected to the vessel. Additionally, applying a roto translational matrix to the rigid body of the vessel makes, the total net mooring force on the body's center of gravity can be defined.

It should be noted that the mooring model presented here involves some approximations, as the equations only refer to translational degrees of freedom. OrcaFlex© can also include other features such as bend and torsional moments. For a comprehensive investigation of the software features, please refer to Orcina (2020).

In the presented model each mooring line is divided into a series of segments, chosen to be 61 after a sensitivity analysis, and it is modeled accounting only for its axial and torsional properties. Together with the sensitivity analyses of the number of segments, also the time step sensibility was examined and finally the simulation time step was set to 0.01 s. The objective of the sensitivity analysis is to determine an accurate numerical setup while minimizing computational time. The parameters monitored during the sensitivity study are the device pitch response and the mooring line tensions. For this purpose, numerical simulations were conducted for the extreme regular wave, described in Table 8, as follows:

- Firstly, a reasonable number of mooring line segments was defined, in this case seventy, and each simulation with this mooring line discretization was performed with a different time step. 10 simulations were performed with time steps ranging from a minimum of 0.005s–0.1s with a step of 0.005s. The pitch motion and the mooring line force amplitude were computed for each simulation. The time step was chosen when the amplitude of the i-th simulation was up to 99% of the value related to the simulation with the minimum time step.
- Once the time step was selected, the same procedure was applied to the mooring line discretization, where the segments' length ranged between a minimum of 0.5m and a maximum of 5m with a step of 0.1m. The number of segments was then obtained by dividing the mooring line length by the length of each segment.

Orcaflex© allows multiple ways of wave generation: a wave spectrum can be defined, or time histories can be implemented. In this paper, the upscaled and reconstructed time histories acquisition from experimental tests have been implemented in the software. For each irregular wave the time history was reconstructed through a harmonic decomposition which led to N harmonics whose superposition in time gives exactly the required time history but allows to drastically reduce the computational cost.

5. Experimental setup

The towing tank is 135 m long, 9 m wide and 4.2 m deep, with a wave maker able to generate regular and irregular waves with a period range of 0.8–4 s and wave amplitude range of 0.08–0.20 m. For the experimental setup, to scale the environmental conditions in terms of water depth, a shoal draft artificial seabed has been built and positioned in the towing tank at a depth of 1.28 m corresponding to 32 m at full scale. As shown in Fig. 8, the 1:25 model is placed at 65m far from the wave maker.

Two measurement campaigns have been carried out:

- Wavemaker calibration without the model: the carriage is positioned to have the gauges around the chosen position of PEWEC. This configuration aims to verify the wave repeatability and to calculate the wave height and period of the real wave impacting on the device. All the calculations made for regular and irregular waves are relative to the elaboration of the time series of wave probe 5, as in Fig. 8. The scope of the other wave probes is to verify that the wave is planar and to understand the influence of the PEWEC device in the wave field (Niosi et al., 2021)
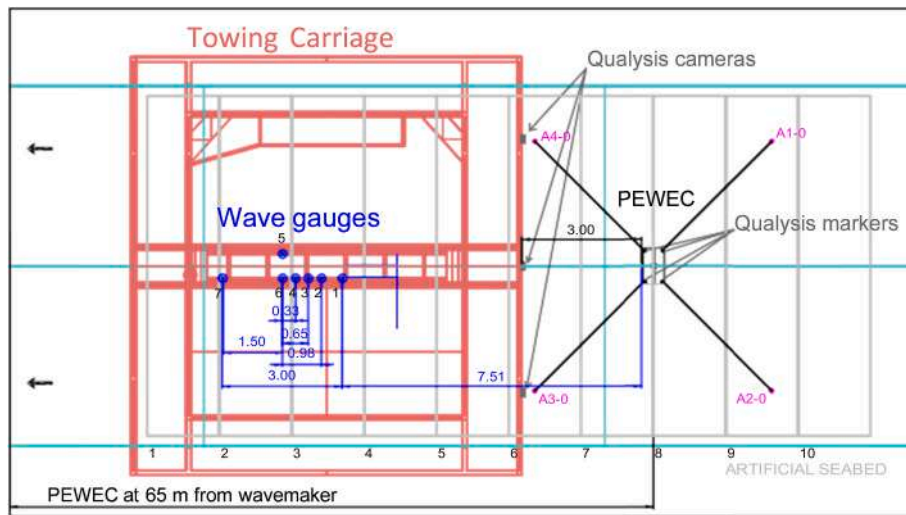
Fig. 8. Experimental setup.

- Operating and extreme conditions: PEWEC is moored at its position on the artificial seabed and the towing carriage is positioned between the wavemaker and the model (with a 3 m distance between the back of the carriage and the bow of the prototype), as shown in Fig. 8.

5.1. Artificial seabed

The shoal draft artificial seabed, shown in Fig. 9, is 18m long and 8.50 m wide. It has been divided into 20 fiberglass panels connected by steel junctions: each of them is 1.8 m long, 4.25 m wide, and 0.25 m thick, and has an X structure on the lower side to stiffen the panel. The panels have been set in two columns filling the whole tank width and are laid in the longitudinal direction in 10 rows to achieve the designed 18 m length. The seabed is fixed to the tank sides through 50 brackets. Each bracket has a sliding part that can be moved vertically to achieve the desired depth.

The artificial seabed has been stiffened and fixed in the desired position throughout the following fittings:

- A transversal structure, between each row of panels, to increase the flexural stiffness of the rows.
- Steel wires, fixed from the center or middle of the panels to each side of the tank, aimed at avoiding transversal motions and increasing the vertical stiffness too.
- Steel wires, set longitudinally along each side of the tank, from each of the four angles of the whole seabed, to avoid translational motions through their own ten sile strength.

- All the panels have been connected by C-shaped fittings bolted to the brackets so that the seabed can be considered as a whole body.
- Steel chains, set longitudinally from each of the four angles of the whole seabed along each side of the tank, further contribute to keeping the panels together, avoiding movements between each of them.

All reinforcing structures are positioned to avoid interference with the prototype motions when tested in waves. After positioning and stiffening the artificial seabed, the whole structure has been tested to measure the deformation response in the z direction along the longitudinal centreline of the structure. The deformation was increasing with high wavelengths, while negligible changes occurred with increasing the wave height. The greatest measured deformation reached about 1 cm for long waves (frequency less than 0.4Hz), while for shorter waves the deformations were negligible.

5.2. Experimental configuration of the mooring system

The model was tested in regular and irregular waves for three headings of incident waves: 0° (head sea), 45° (bow quartering), and 90° (beam sea). All three mooring arrangements have been set up on the artificial seabed, but only the results concerning head sea conditions are reported in this work, the other wave headings can be found in Fenu et al. (2022). The considered head sea configuration is represented in Fig. 10, where the x and y coordinates of the anchors position are given with reference to the center of the model. The other wave direction will be detailed in future works.

Fig. 9. Qualisys cameras position and shoal artificial seabed.

5.3. Wave generation and calibration

Seven Akamina© wave probes have been placed on the towing carriage with relative distances as shown in Fig. 8. Gauges 1, 2, 3, 4, 5 and 7 have been placed on the same y coordinate to analyse the wave height variations on the artificial seabed, while gauge 6 has been set at the same longitudinal position as gauge 5 with symmetrical y coordinate with respect to the x axis. During the calibration tests, the carriage was positioned to have the redundant gauges, 5 and 6, in the chosen position of the device. The complete set of tested regular and irregular waves are summarised in Tables 4–6. Operative regular waves have been chosen with wave periods in the range of 4–7.5 s, with step of 0.5 s, in full scale, which are the most probable waves in the Mediterranean Sea. Around the PEWEC resonance frequency, tests were performed with increment 0.2s to properly describe the device behaviour. Wave heights have been determined to have waves with steepness of 1:50, as in Table 4, and 1:30, as in Table 5.

Operative irregular waves have been chosen from the scatter tables obtained from the 50 years statistics of Rete Ondametrica Nazionale (RON) data post-processing, for Pantelleria site. Four peak periods were chosen (between 5 and 8 s) as the most probable according to the scatter shown in Fig. 11. The green and red line refer respectively to wave with iso-steepness equal to 1:50 and 1:30. The JONSWAP spectrum has been chosen as representative of the Mediterranean Sea in the experimental set up.

To define the extreme waves, it is necessary to determine the environmental contour (EC) related to a return period of 100 years. The EC reported in Fig. 12 determined following the DNV-RP-C205 (2014) standard, allowed to select of the extreme wave to simulate. Due to the experimental setup limitations, the severe irregular wave reported in Table 8 was chosen. For what concerns the extreme condition, the regular wave with wave height $H = 1.9 \cdot H_s$ and wave period $T = T_p$ should have been tested, but for experimental setup limitations, the one indicated in Table 8 has been used in experiments.

The experimental data shown in Table 5, Table 6, Table 7 and Table 8 are calculated by post-processing the time domain signal acquired by the wave gauge 5 through the Fast Fourier Transformation for regular waves, and through the reconstruction of the time history of wave elevation for extreme irregular wave.

6. Acquisition system

Two acquisition systems have been used to measure the 6 DOF device motions: Qualysis© optical motion tracking system and IMU (Inertial Motion Unit) onboard system.

For the optical motion tracking, 3 cameras have been placed on the carriage back facing the device, as represented in the top view of Figs. 8 and 9 and detailed in Fig. 13.

Five Qualisys© markers have been placed on PEWEC deck to assure an accurate definition of the 3D rigid body and measurements. The Qualisys acquisition system captures both rotational and translational motions of the device by setting the position X_o (0,0,0) as the starting position of the PEWEC in its moored static position.

The onboard acquisition system consists of a National Instruments© compact RIO (cRIO) controller and analogic and digital I/O modules, powered by batteries and equipped with a Wi-Fi router for real-time transmission of the acquired sensor data. The cRIO controller has been programmed in the LabVIEW© environment to acquire data from the transducers with a frequency of 20 Hz. A simplified scheme of its architecture is shown in Fig. 14 and the complete list of components is presented in Table 9.

The cRIO module acquires the data coming from an Xsens MTI-30 (IMU), positioned inside the hull to measure rotational motions, data from the four load cells and data from the 27 pressure sensors.

During the tests, the two acquisition systems were synchronized through a digital trigger signal generated by the cRIO controller.

To read the data in physical units of measure, load cells and pressure sensors were calibrated to obtain loads and pressures from electric signals. All the gain and offset values of the sensors installed on the hull are reported in Table 10. A single characteristic was used for the 27 pressure transducers, containing the average of the gain and offset values of each transducer while each load cell had different gain and offset.

To validate the pressures in extreme events through CFD simulations, 27 pressure sensors were applied by piercing the hull and gluing them in place with two-component glue, which ensured the hull's watertight integrity. In this paper, results related to pressures are not reported.

The load cells were connected to the carabiners with eyebolts at the four corners of the hull and linked directly to the mooring lines. The cells were numbered as the corresponding mooring line to which they were connected. Fig. 15 shows the top view of the positions and numbers of the sensor.

7. Numerical model validation

The numerical simulations performed in Orcaflex© have been validated with experimental tests by the following procedure: linearized viscous damping coefficients (obtained from experimental decay tests) have been inserted in the simulations; simulated and experimental mooring static characteristics have been compared; the validation of the numerical model has been performed in operative and extreme regular and irregular waves.
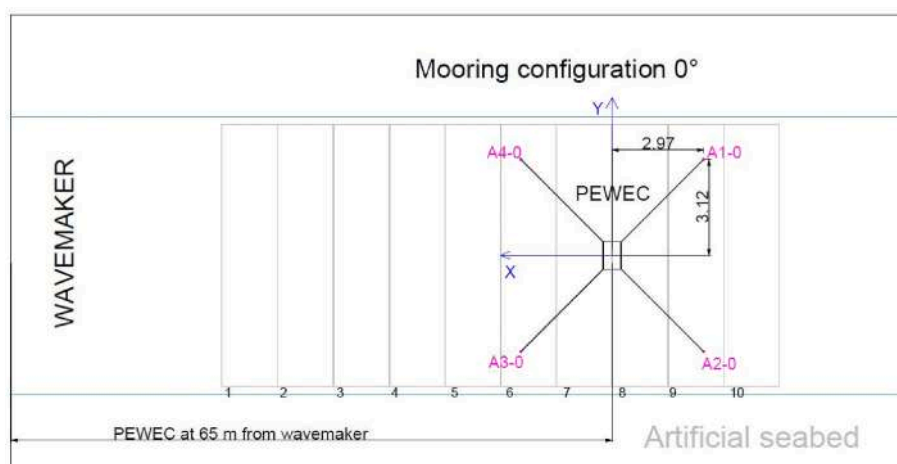

Fig. 10. Mooring configuration for head sea waves.

Table 5
Regular waves in full scale and measured in experiments with steepness 1:50.

Test ID	H	T	H_MOD-TARGET	T_MOD-TARGET	H_MOD-EXP	T_MOD-EXP	H_Diff	T_Diff
	(m)	(s)	(cm)	(s)	(cm)	(s)	(%)	(%)
RW$_{01}$	1.04	4.5	4.17	0.9	4.54	0.90	8.7	0.1
RW$_{02}$	1.29	5	5.15	1	5.11	1.00	0.8	0.0
RW$_{03}$	1.56	5.5	6.24	1.1	6.03	1.10	3.3	0.1
RW$_{04}$	1.85	6	7.42	1.2	7.38	1.20	0.5	0.0
RW$_{05}$	2.04	6.3	8.17	1.26	7.85	1.26	3.9	0.1
RW$_{06}$	2.18	6.5	8.71	1.3	8.61	1.30	1.1	0.0
RW$_{07}$	2.31	6.7	9.24	1.34	9.43	1.34	1.9	0.0
RW$_{08}$	2.52	7	10.10	1.4	9.91	1.40	1.8	0.0
RW$_{09}$	2.90	7.5	11.58	1.5	11.29	1.50	2.5	0.0

Table 6
Regular waves in full scale and measured in experiments with steepness 1:30.

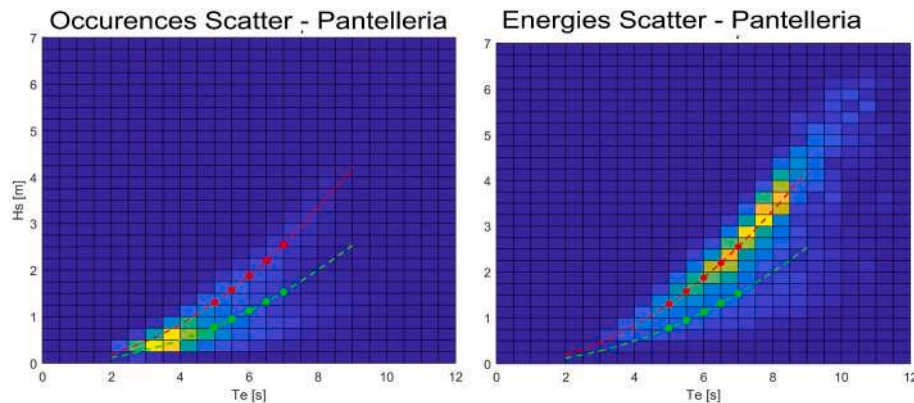| Test ID	H	T	H_MOD-TARGET	T_MOD-TARGET	H_MOD-EXP	T_MOD-EXP	H_Diff	T_Diff
	(m)	(s)	(cm)	(s)	(cm)	(s)	(%)	(%)
RW$_{10}$	0.50	4	2.00	0.8	2.13	0.80	6.7	0.0
RW$_{11}$	0.63	4.5	2.53	0.9	2.32	0.90	8.4	0.0
RW$_{12}$	0.78	5	3.12	1	3.11	1.00	0.4	0.0
RW$_{13}$	0.95	5.5	3.80	1.1	3.91	1.10	2.9	0.0
RW$_{14}$	1.12	6	4.48	1.2	4.73	1.20	5.6	0.0
RW$_{15}$	1.24	6.3	4.95	1.26	4.99	1.26	0.8	0.0
RW$_{16}$	1.32	6.5	5.28	1.3	5.51	1.30	4.3	0.0
RW$_{17}$	1.40	6.7	5.60	1.34	5.97	1.34	6.6	0.0
RW$_{18}$	1.53	7	6.12	1.4	6.01	1.40	1.8	0.0
RW$_{19}$	1.75	7.5	7.02	1.5	6.78	1.50	3.3	0.0

Fig. 11. Wave Scatter used for experimental waves definition.

7.1. Roll and pitch free decay tests

To set accurate simulations in Orcaflex© environment, the damping coefficients of the vessel calculated through the potential flow theory, should be corrected taking into account the viscous terms determined experimentally or by CFD simulations. In this case, a set of experimental tests of roll and pitch free decays have been performed, analyzed, and post-processed with the aim to assess the linearized extinction coefficient of the free decay curve to implement in the numerical model. In Fig. 16 and in Fig. 17 the measured decay curves for pitch and roll are shown. It can be observed that free decay oscillations are not filtered out by averaging, and the initial static values of pitch and roll are not zero due to the slight asymmetry of the model. The static value of roll motion is around 2° due to the arrangement of internal components in the model. This offset is reduced by the weight of the chains on the prototype when the device is moored and does not affect the device motions in head waves since the pitch and roll motions are uncoupled. Furthermore, a static offset of the pitch and roll angles does not influence the calculated damping values.

Once the free decay time histories for pitch and roll motion are available, adopting the procedure detailed in Mancini et al. (2018) and Fontana et al. (2020), the damped period T_D, the linear term and the quadratic extinction coefficients are calculated through a linear regression and reported in Table 11.

These coefficients are used to calculate the viscous damping linear and quadratic terms, as reported in equations (9) and (10) and set as input in the numerical model. It's worth to underline that these damping values refer to the natural frequency of the device, but they are considered constant values in the Orcaflex© model.

$$Bv_{lin} = 2\alpha \cdot (I_{ii} + A_{ii}(\omega_r)) \tag{9}$$

$$Bv_{quad} = \beta \cdot (I_{ii} + A_{ii}(\omega_r)) \tag{10}$$

where I_{ii} is the mass matrix term referred to the i DOF, $A_{ii}(\omega_r)$ is the added mass term calculated by BEM software of the i DOF at the resonant frequency.
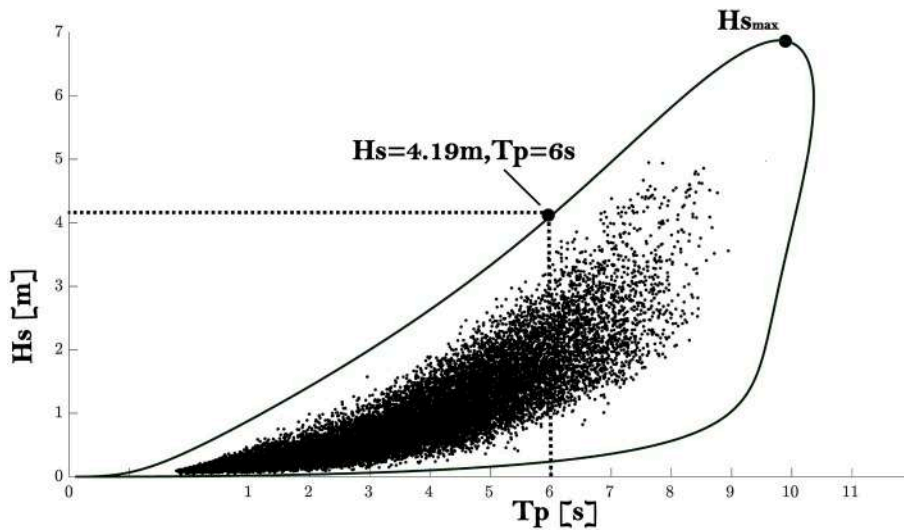
Fig. 12. Environmental contour (EC) for the Pantelleria site in Mediterranean Sea.

Table 7
Irregular waves in full scale and measured in experiments.

Test ID	H_s	T_p	$H_{MOD-TARGET}$	$T_{MOD-TARGET}$	$H_{MOD-EXP}$	$T_{MOD-EXP}$	H_Diff	T_Diff
	(m)	(s)	(cm)	(s)	(cm)	(s)	(%)	(%)
IRR_{01}	1.29	5	5.16	1	5.11	0.99	0.98	0.4
IRR_{02}	1.86	6	7.44	1.2	7.24	1.17	2.64	2.1
IRR_{03}	2.53	7	10.12	1.4	9.75	1.40	3.61	0.2
IRR_{04}	3.3	8	13.2	1.6	12.65	1.60	4.20	0.2
IRR_{05}	0.78	5	3.12	1	3.19	1.02	2.24	2.1
IRR_{06}	1.12	6	4.48	1.2	4.42	1.15	1.23	3.8
IRR_{07}	1.53	7	6.12	1.4	5.86	1.35	4.20	3.7
IRR_{08}	2.00	8	8.00	1.6	8.10	1.60	1.21	0.2

Table 8
Extreme waves in full scale and measured in experiments.

Test ID	H_s	T_p	H/H_s MOD-TARGET	T/T_p MOD-TARGET	H/H_s MOD-EXP	T/T_p MOD-EXP	H_Diff	T_Diff
	(m)	(s)	(cm)	(s)	(cm)	(s)	(%)	(%)
RW_{EX}	4.50	6	18.00	1.2	17.62	1.2	2.1	0.0
IRR_{EX}	4.19	6	16.78	1.37	16.20	1.2	3.4	14.7

7.2. Static pull-out test

A key part when designing a WEC is the influence of the mooring on the device. Fig. 18 shows the trend of the forces of the lines under tension as a function of the device longitudinal position during the static pull-out tests. The tests have been carried out by tying ropes to the PEWEC ogives and pulling them up to the maximum excursion given by the extension of the mooring lines. While the PEWEC was pulled, the forces measured by load cells have been acquired. The static pull-out tests have been performed using the synchronized acquisitions of the Qualisys© for the surge displacement and the cRIO acquisition system for the load cell measurements. The same process was simulated in Orcaflex© and the comparison of numerical against experimental results is given in Fig. 18. The static characteristics of the mooring are perfectly replicated by the software as shown in Figs. 18 and 19. The aim of the pull-out test is to assess the static stiffness of the mooring and ensure that the scaling has been executed accurately.

7.3. Operative regular waves

The PEWEC responses in regular operative wave conditions were performed in full-scale environment, as reported in Tables 5 and 6. Two steepness have been tested: 1:50 and 1:30 (11 waves for 1:50 and 9 for 1:30). The steepness is defined as $st = \frac{2 \cdot A_w}{\lambda}$ where, $2 \cdot A_w$ is the wave height and λ is the wavelength.

Response Amplitude Operators (RAOs) have been calculated for surge, heave, and pitch motions as follows:

$$RAO_{Surge} = \frac{\eta_1}{A_w} \tag{11}$$

$$RAO_{Heave} = \frac{\eta_3}{A_w} \tag{12}$$

$$RAO_{Pitch} = \frac{\eta_5}{k \cdot A_w} \tag{13}$$

where A_w is the wave amplitude, n_1, η_3, η_5 are respectively the surge, heave and pitch amplitudes and $k = 2 \cdot \pi / \lambda_w$ is the wave number. The comparison between numerical and experimental results of the three motions is given for both wave steepness, as reported in Fig. 20, Fig. 21, and Fig. 22. The figures show the DOF RAO on the left y-axis and the relative error, plotted with vertical bars, between experimental and numerical values on the right y-axis. The surge motion is characterized by multiple frequency components (wave frequency and low mooring frequencies). Pitch and heave motions are mainly excited by the wave frequency. Roll, yaw, and sway motions have negligible influence in head sea waves. Numerical simulation results are in good agreement with experimental ones, especially for pitch motion which mainly influences the device productivity. As the wave steepness increases, the
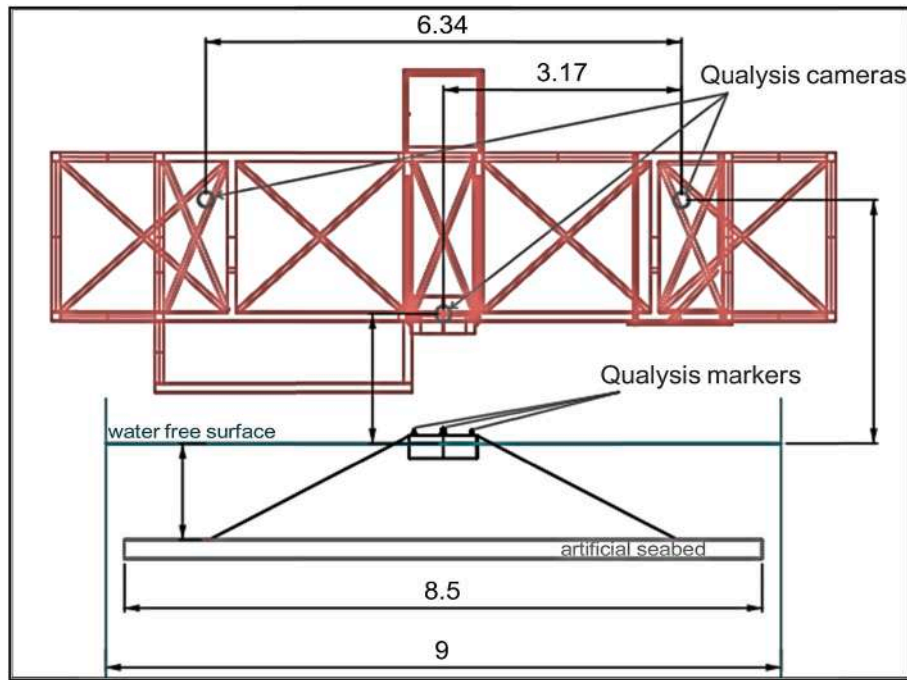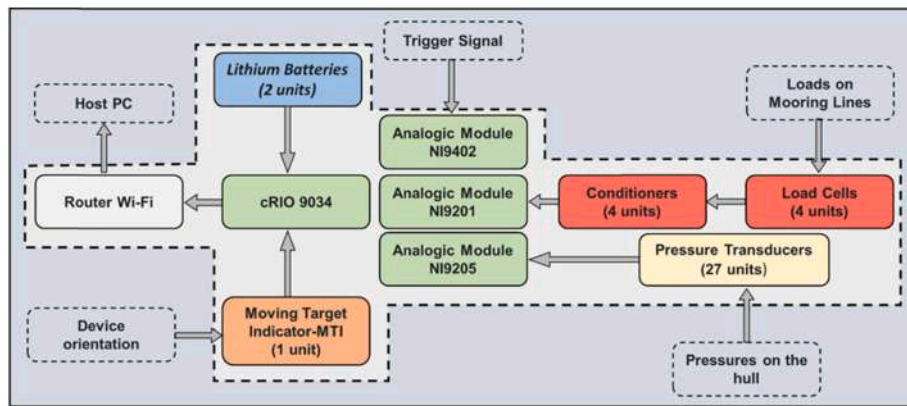
Fig. 13. Qualisys© setup scheme.

Fig. 14. System acquisition block scheme.

Table 9
Acquisition system on board of PEWEC.

Component	Producer	Model	Quantity
Controller	NI	cRIO 9034	1
Digital Modules	NI	NI9401	1
Analogic module for pressures	NI	NI9205	1
Analogic module for loads	NI	NI9201	1
Lithium batteries	LaserElectronic	12V 25AH 25000Ma	2
Router Wi-Fi	TPlink	EAP225	1
Load cell (100 lbs)	Futek	lsb210 – 100 lb	4
Load cell conditioner	Futek	IAA100	4
Pressure transducer	NXP	MPVZ5010GW7U	27
IMU	Xsens	MTI-30	1

Table 10
Transformation ratios of on-board sensors.

Components	Features	Gain	Offset
Load Cell 1	Load [Kg] = Gain * Tension [V] + Offset	3.9808	0.0323
Load Cell 2	Load [Kg] = Gain * Tension [V] + Offset	3.9307	0.1511
Load Cell 3	Load [Kg] = Gain * Tension [V] + Offset	4.0049	0.1368
Load Cell 4	Load [Kg] = Gain * Tension [V] + Offset	4.0003	−0.0444
Pressure Sensors	Pressure [KPa] = Gain * Tension [mV] + Offset	0.0023	−0.5444

numerical model. The values refer to the main amplitude of the fairlead tension time history of each regular wave tested and are reported only for the most stressed Load Cells 3 and 4, since they are placed at the bow as shown in Fig. 15. The relative error between experimental and numerical values is reported in the error bars in the y-axis on the right. The results are in good agreement with the numerical model.

numerical model slightly overestimates the pitch motion. The numerical error increases for waves with high steepness and with a period close to the device resonance which is in accordance with the linear theory.

Mooring tensions at the hull attachment points (where the load cells are located) are represented in Fig. 23 for both the experimental and the
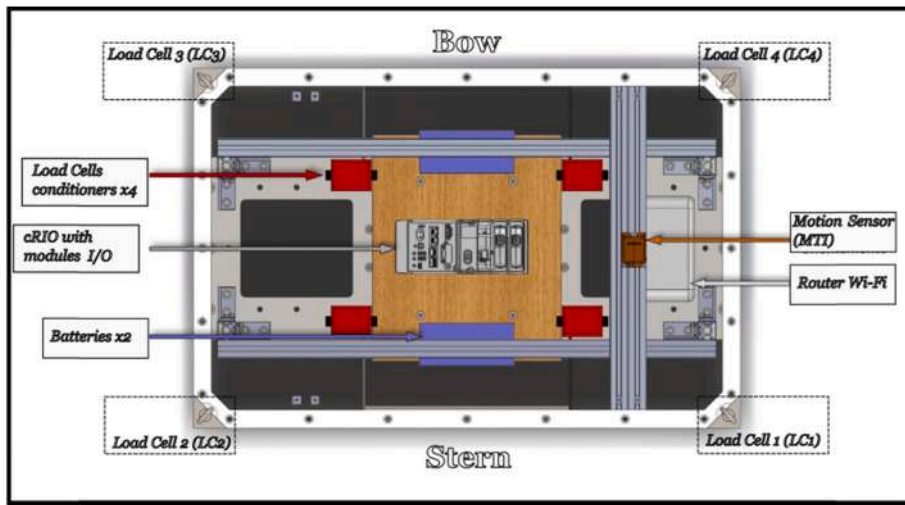
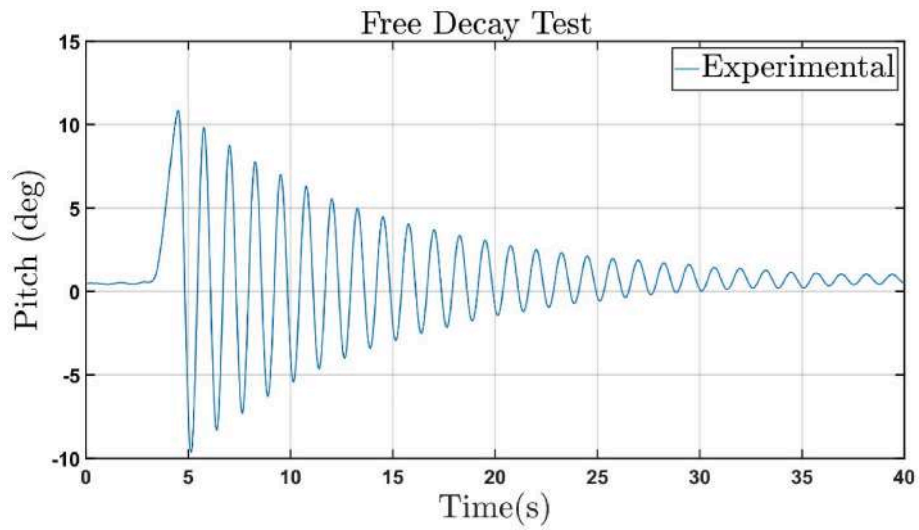**Fig. 15.** Top view of acquisition system sub-modules disposition inside the prototype.

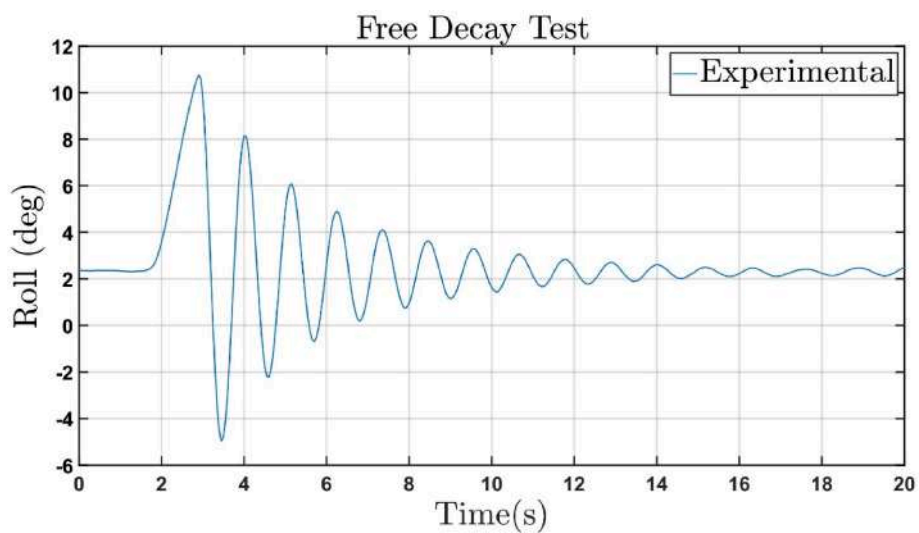**Fig. 16.** Pitch free decay test.

Fig. 17. Roll free decay test.

Table 11
Comparison of damped period and extinction coefficients results by experimental free-decays.

Free Decay	$T_{D\text{-MODEL}}$ (s)	T_D (s)	α (1/s)	β (−)
Pitch	1.25	6.25	0.154	0.031
Roll	1.13	5.58	0.042	0.914

7.4. Operative irregular waves

All the tests shown in Table 7 were carried out to characterize the response of the device to irregular waves and, as mentioned previously, the acquired time history of wave elevation was implemented in the numerical Orcaflex© model. The validation of the device kinematics and of the loads on the lines were carried out through statistical and frequency analyses. Fig. 24, Figs. 25 and 26 show the average heave, pitch, and surge RAOs respectively, calculated using the experimental and numerical data. The average RAO has been calculated by the following methodology:

- Pitch and wave height signals are read over time for each irregular wave tested.

- The Fourier transformation is applied to both signals, purified from the mean value, to pass from time to frequency domain.
- The ratio between the respective absolute values of the Fourier transforms is calculated.
- The ratio of the two signals for all the eight irregular waves are averaged at each frequency.

The steps listed above can be written in Equations (14) and (15):

$$RAO_{wave_i} = \frac{fft(x_{5i}(t))}{fft(\eta_{wavei}(t))}, with\ i = 1:8 \tag{14}$$

$$RAO_{mean}(\omega) = \frac{\sum_{i=1}^{N_{waves}} RAO_{wave\,i}(\omega)}{N_{waves}}, with\ N_{waves} = 8 \tag{15}$$

The numerical model correctly estimates pitch and heave motions while it is less accurate for the surge motion. This can be partially attributed to the uncertainties of the experimental setup such as the topological distribution of the clump weights on the artificial seabed at the start of each test and the estimation of the drag coefficients of the chains or the actual level of the seabed. As discussed in Wright et al. (2022), predictions of slow drift motions still did not reach a satisfactory level with literature on the topic, showing a gap in the current state of
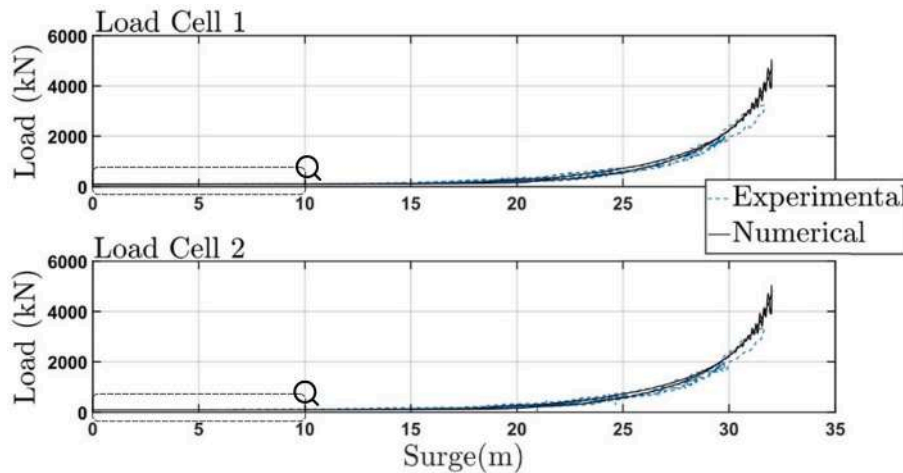
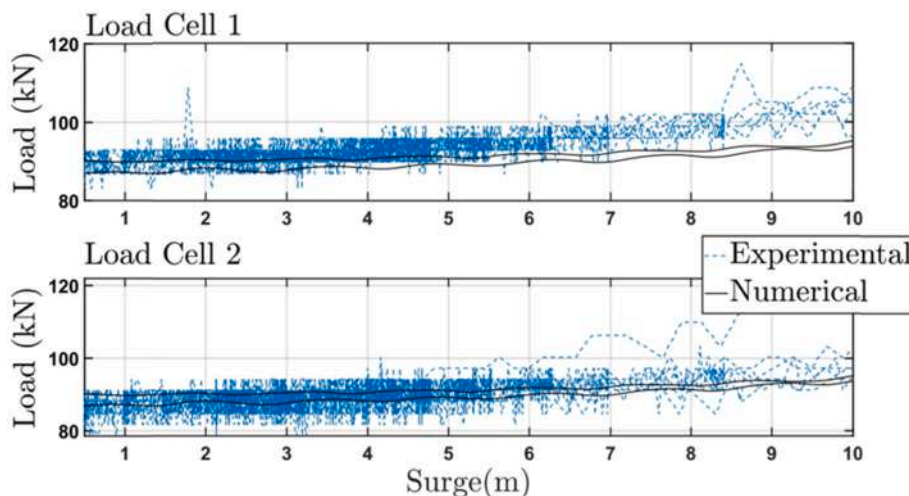

Fig. 18. Fairlead Tension during pull-out test.

Fig. 19. Zoom of the fairlead tension during pull-out test in the operative range highlighted in Fig. 18.
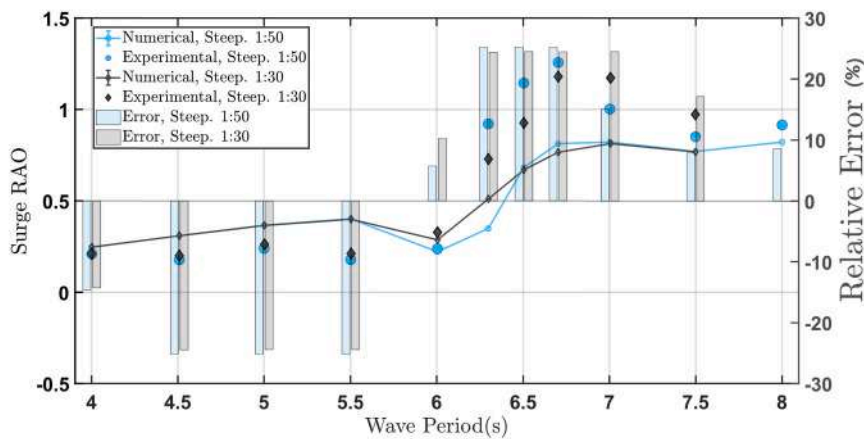
Fig. 20. Experimental and numerical Surge RAO in 1:50 and 1:30 steep regular waves (left y-axis), Relative error between Experimental and numerical values (right y-axis).
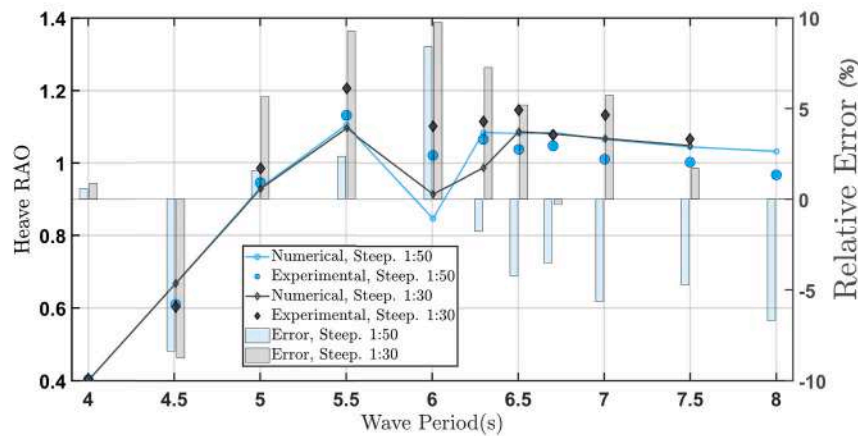

Fig. 21. Experimental and numerical Heave RAO in 1:50 and 1:30 steep regular waves (left y-axis), Relative error between Experimental and numerical values (right y-axis).
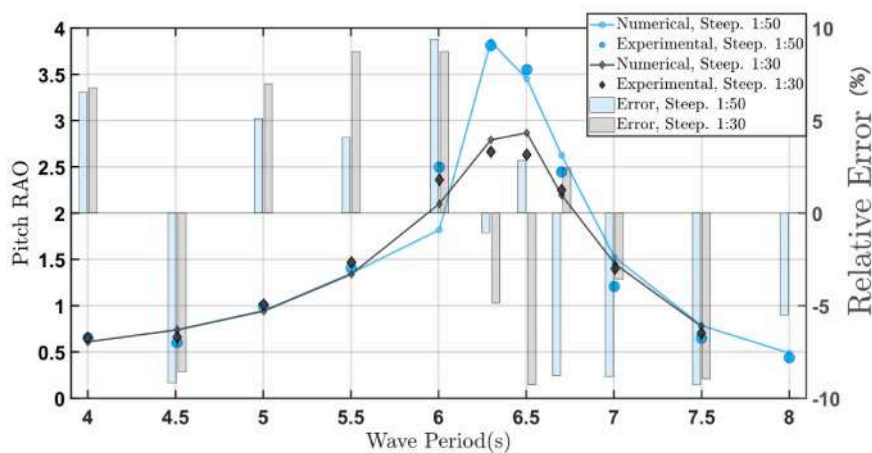

Fig. 22. Experimental and numerical Pitch RAO in 1:50 and 1:30 steep regular waves (left y-axis), Relative error between Experimental and numerical values (right y-axis).

the art. Possible reasons behind the errors are the calculation of second-order forces by potential flow theory and the need for a correction to match those calculated in experimental wave basin testing, having viscous drag coefficients that are amplitude and frequency dependant, and accounting for the wave–current effect on both excitation and damping forces.

Figs. 27 and 28 show the comparison between the synchronized time histories of pitch motion related to the experimental acquisition and the
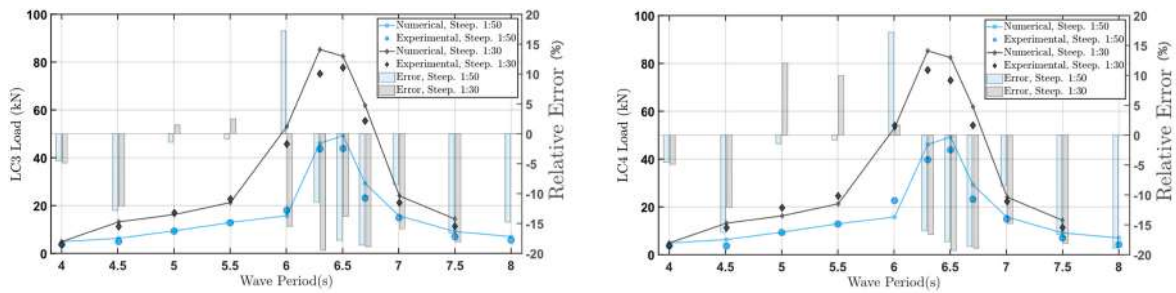
Fig. 23. Experimental and numerical Load Cell Amplitudes of starboard mooring lines in 1:50 and 1:30 steep regular waves (left y-axis), Relative error between Experimental and numerical values (right y-axis).
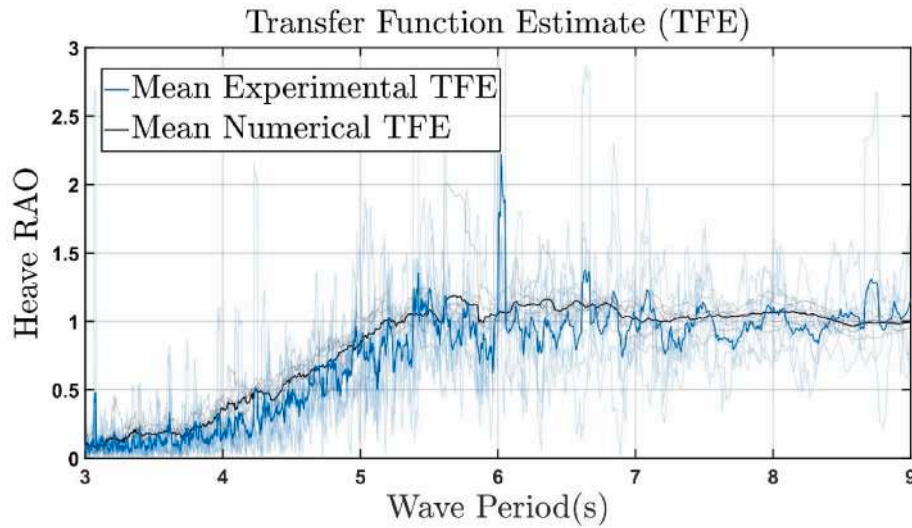

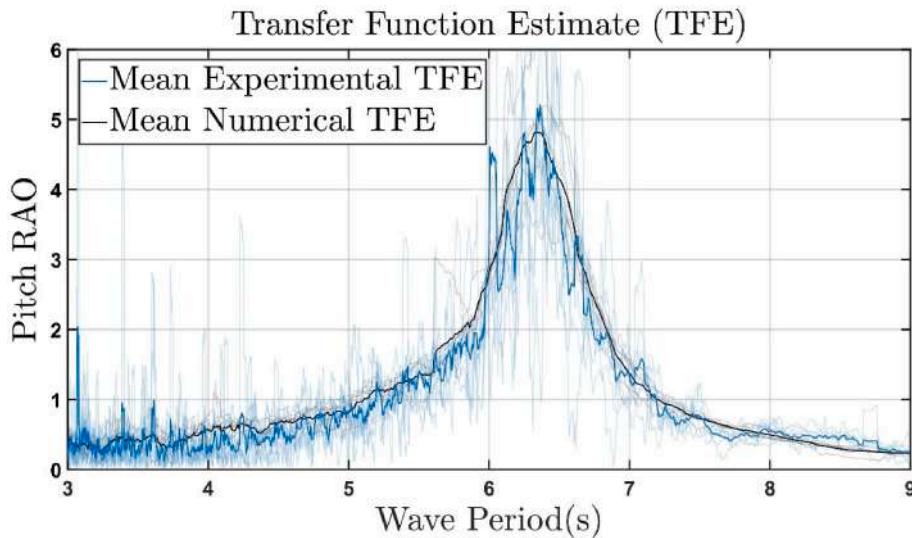**Fig. 24.** Average heave RAO using the experimental acquisition and the Orcaflex© numerical model.

Fig. 25. Average pitch RAO using the experimental acquisition and the Orcaflex© numerical model.

numerical simulations for irregular waves 02 and 06 (Table 5), whose periods are close to the device resonance. It can be noted that the validation in terms of statistical values (STD, standard deviation value of the signal) is consistent, and the superposition of the signals in the time domain (obtained for the reasons mentioned above by slipping one of the two signals in post-processing) provides excellent results.

Taylor diagrams obtained from the two pitch time histories are shown in Fig. 29. In each diagram the standard deviations (STD), the Centered Root Mean Square Error (RMSD) and the correlation coefficient (CC) of the two signals are reported. These three parameters are respectively calculated with Equations (16)–(18) and reported in Table 12:
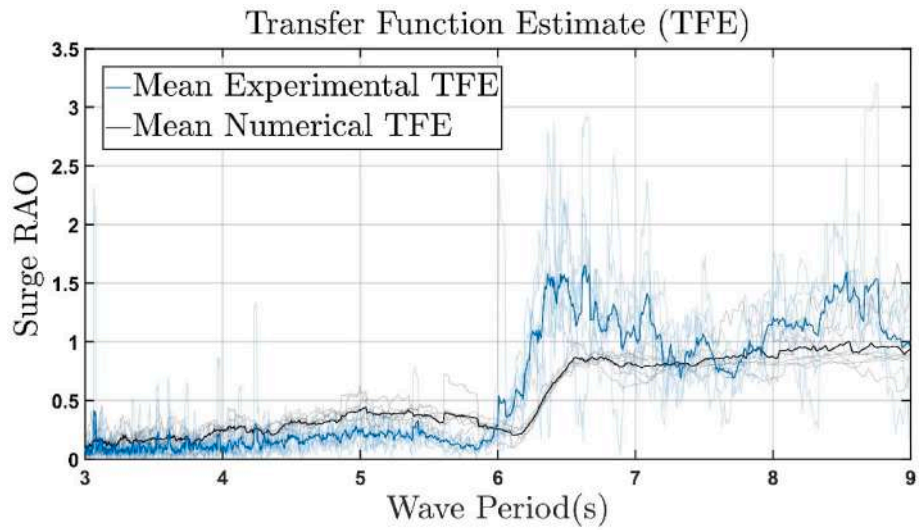
Fig. 26. Average surge RAO calculated using the experimental acquisition and the Orcaflex© numerical model.
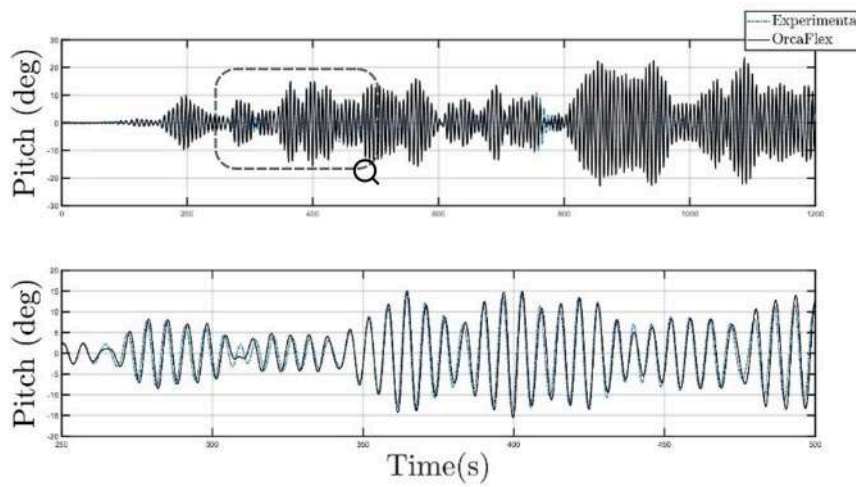

Fig. 27. Time histories of pitch motion comparison for irregular wave Irr. 02: experimental vs numerical.
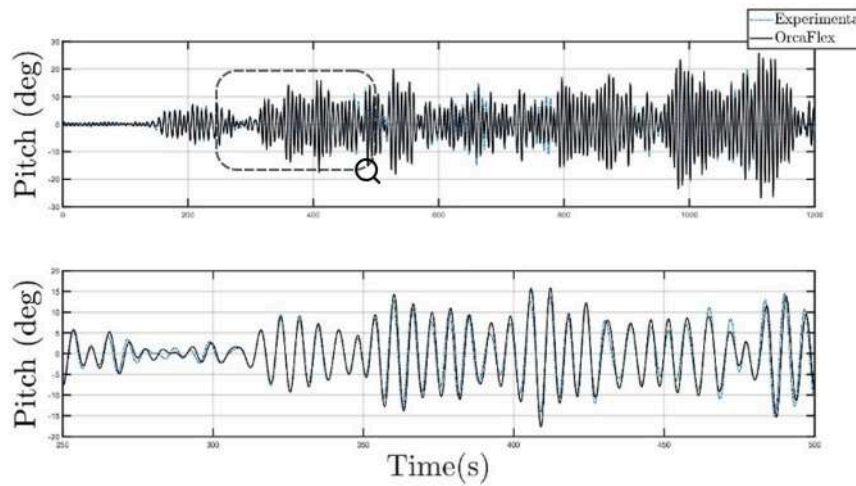

Fig. 28. Time histories of pitch motion comparison for irregular wave Irr. 06: experimental vs numerical.
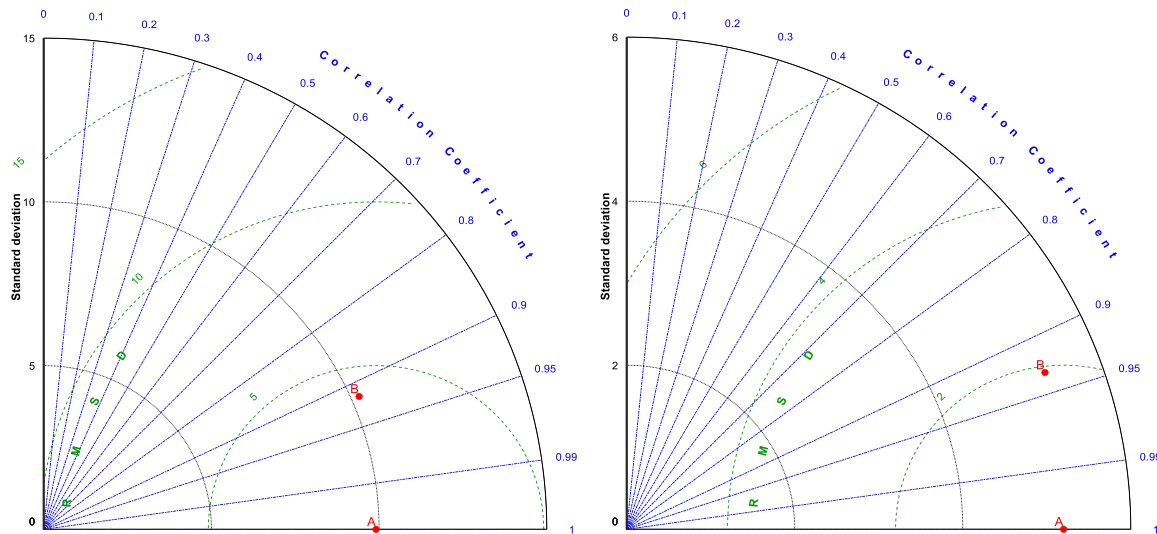
Fig. 29. Taylor diagrams related to pitch motion for wave irr. 02 (on the left) and irr. 06 (on the right).

Table 12
Root Mean Square Deviation, Standard Deviation error and Correlation Coefficient for surge heave and pitch motion: experimental VS numerical.

DOF	Surge			Heave			Pitch		
	RMSD	STD_{Err} (%)	CC	RMSD	STD_{Err} (%)	CC	RMSD	STD_{Err} (%)	CC
IRR_{01}	1.8	22.0	0.86	0.15	2.1	0.83	1.9	2.5	0.93
IRR_{02}	2.4	13.7	0.74	0.24	0.4	0.81	3.9	6.8	0.92
IRR_{03}	1.8	3.2	0.84	0.17	1.4	0.96	3.0	6.2	0.96
IRR_{04}	2.7	4.8	0.6	0.32	1.9	0.91	4.1	3.3	0.92
IRR_{05}	2.1	7.7	0.57	0.15	1.3	0.95	2.1	4.8	0.96
IRR_{06}	1.9	5.2	0.58	0.14	4.1	0.87	2.6	5.2	0.95
IRR_{07}	1.7	7.4	0.52	0.21	2.4	0.84	2.6	4.7	0.94
IRR_{08}	1.8	15.7	0.52	0.15	1.5	0.95	2.2	4.5	0.95

$$STD(C \bigvee C_r) = \sqrt{\frac{\sum\left[(C \bigvee C_r) - mean((C \bigvee C_r))\right]^2}{N}} \qquad (16)$$

$$RMSD = \sqrt{\frac{\sum[\{[C - mean(C)] - [C_r - mean(C_r)]\}\hat{2}]}{N}} \qquad (17)$$

$$CC = \sqrt{\frac{\sum[[C - mean(C)] \cdot [C_r - mean(C_r)]]}{N \cdot STD(C) \cdot STD(C_r)}} \qquad (18)$$

In Table 12, the second column of each motion, called $STD_{err}(\%)$, is calculated as the relative error between the numerical model STD and the experimental one. It can be noticed that the errors are in average higher for the surge motion than for heave and pitch. For heave and pitch motions both values in terms of relative error on STD and CC are within 5% and 90%. It must be underlined that the time histories synchronization was done starting from the wave elevation signals in post-processing.

7.4.1. Design load estimation

The aim is to validate the distributions obtained for each experimentally tested wave to assess the design load with the numerical model. For the validation of mooring line loads, a statistical approach was adopted as suggested by Niosi et al. (2021).

A great number of simulations should be performed to determine the design load and for each of them, a statistical distribution of loads acting on the mooring line should be identified. The design load can be found by combining all the obtained distributions (one for each realization).

The data used to fit the distribution are obtained by post-processing the time history signal related to the fairlead load for both experimental acquisition and numerical model.

The basis for the extreme values statistics is the maximum response between two successive crossings of the mean (Peak Over Threshold) and is defined as an overall maximum (see Fig. 30).

Global maxima are assumed to be independent stochastic variables, often modeled by a "Generalized Extreme Value" distribution.

A Generalized Extreme Value distribution was used to fit both experimental and numerical data. The fit was performed through the Matlab© distribution application and the data to be fitted are all the values indicated in Fig. 30 as POT. The same approach was used to model extreme conditions fairlead tensions.

The two distributions, for each wave, can be obtained by fitting the POT points of numerical and experimental time histories. The distributions reported in Fig. 31 are related to irregular wave 02 as a demonstrative example.

7.5. Extreme regular waves

For regular extreme waves, the same quantities, namely motions and tensions, and the same procedure of post-processing as for the operating waves are considered. As seen in Fig. 32, the numerical model overestimates the pitch response of the device because it does not consider viscous or non-linear effects due to the variation of the wet surface and sharp edges. The estimate of the device surge in the numerical model includes a low-frequency response which does not appear in experimental tests. In fact, referring to the surge motion reported in Fig. 32, the discrepancy between the experiment and the numerical simulation can
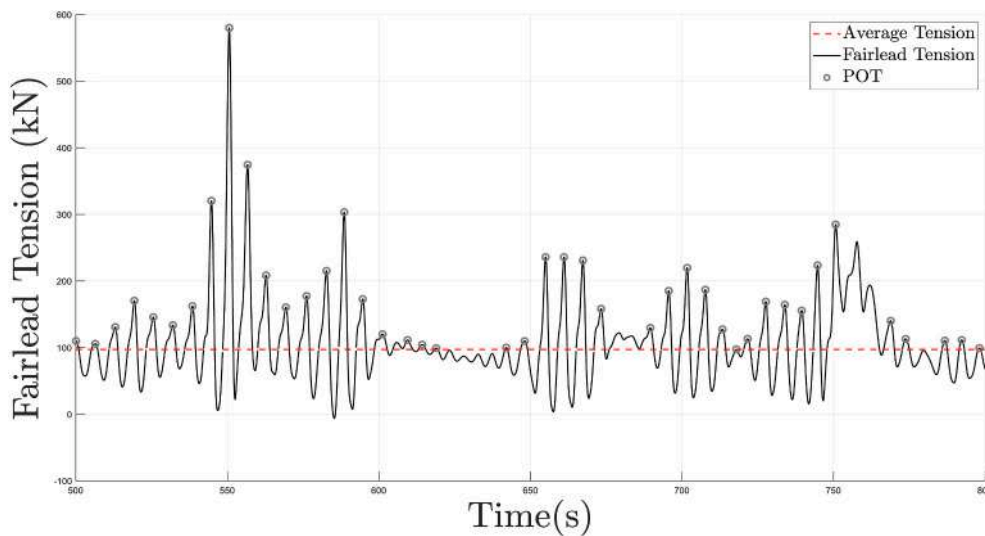
Fig. 30. Peak Over Threshold (POT) DNV procedure: example of a partial time history.
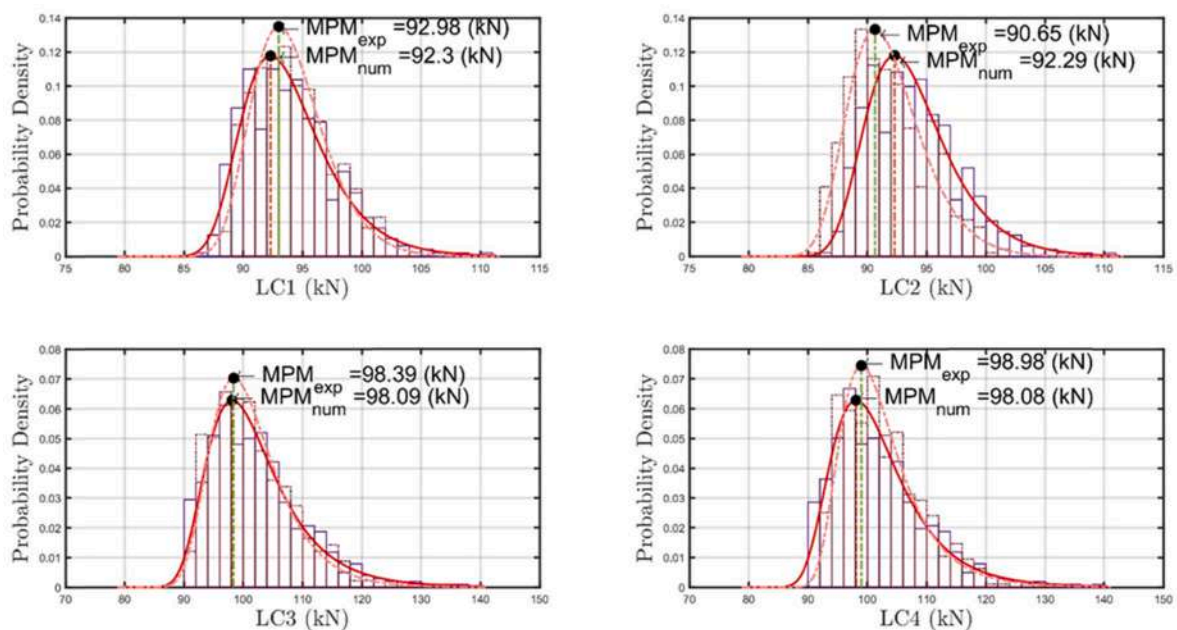

Fig. 31. Numerical and experimental distributions based on DNV procedure: Experimental vs numerical fitted GEV for irregular wave 02.

be attributed to the viscous surge damping not included in the numerical model. The same procedure performed for pitch and roll viscous damping identification should have been performed also for surge. But, while for roll and pitch motion is easy to discern hull-related viscous damping from mooring-related viscous damping because of the presence of a hydrostatic stiffness matrix, for surge motion a more complicated analysis is required, such as CFD simulations or different kinds of experimental tests with constant speed. Since the objective of the paper is to ascertain the device pitch response and the mooring line tensions distributions, only the drag coefficients and added mass coefficients for the mooring lines were included in the numerical model while the linearized hull-related viscous damping was neglected. For the same reason, to smaller extent, loads on mooring lines are overestimated by the numerical simulations due to the increased motions of the device.

7.6. Extreme irregular waves

The numerical simulations, for extreme irregular waves (Table 8), were carried out by implementing three realizations of wave elevation time history. Results obtained by carrying out the Power Spectral Density (PSD) of the experimental acquisition and the numerical model are discussed. Each PSD comparison, reported in the following figures is intended as an average PSD among the three realizations of the extreme wave reported in Table 8. In extreme conditions, the assumptions of linear theory are less applicable, and a greater error is expected in the estimation of motions and loads by the numerical model which uses linear hydrodynamics to solve the motion equation of the device in the time domain. Even if extreme waves are far from the hypotheses of linear theory, the model manages to predict the device motions quite accurately as can be seen from Fig. 33, Fig. 34, Fig. 35. This occurs mainly for two reasons: the first can be associated with the device geometry since the hydrostatic stiffness and wetted surface do not vary
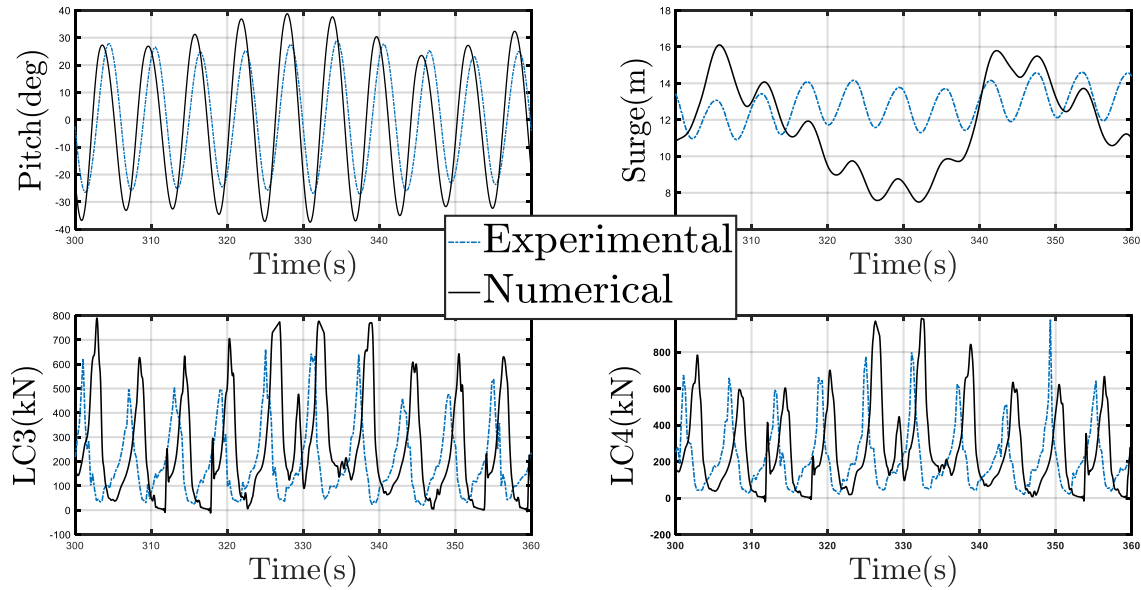
Extreme Regular Wave Results Validation

Fig. 32. Extreme regular wave validation: Pitch motion, Surge motion and fairleads tension at bow mooring lines.
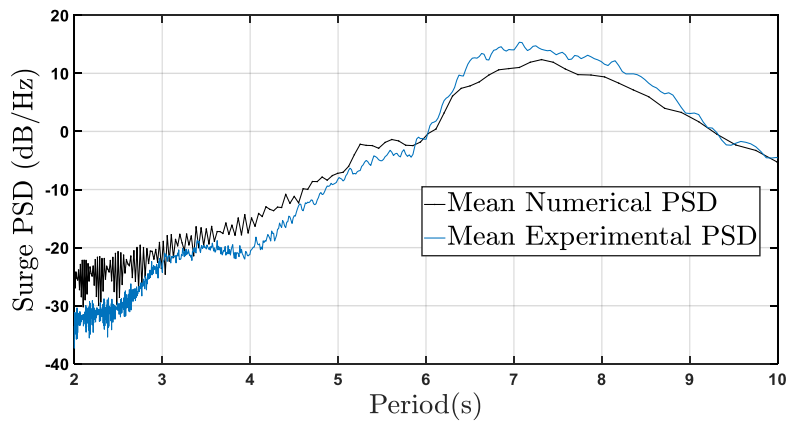

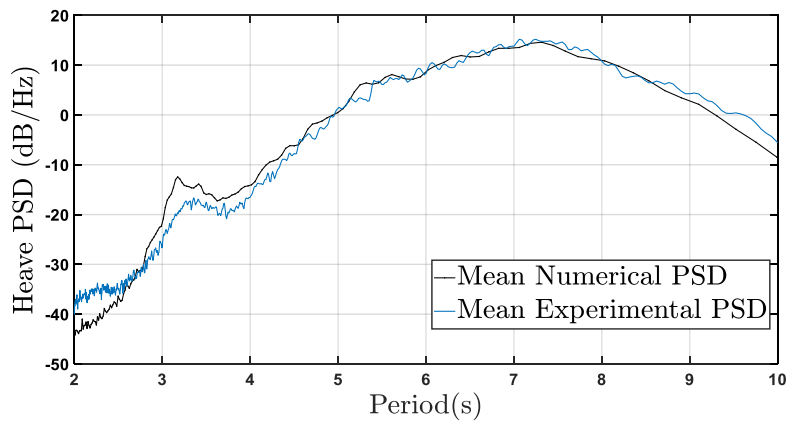**Fig. 33.** Surge PSD: Numerical vs Experimental.

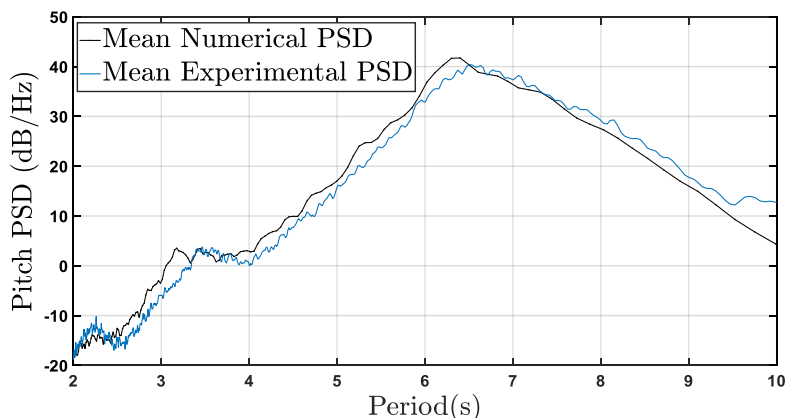**Fig. 34.** Heave PSD: Numerical vs Experimental.

Fig. 35. Pitch PSD: Numerical vs Experimental.

much even for large pitching oscillations the hydrodynamic coefficients and the excitation forces imposed by the wave have small variations. The second reason can be attributed to the linearized viscous damping parameters, added in the model, which consider the viscous effects not modeled in the potential theory used in the classical panel methods.

Figs. 33, Figure 34, and Fig. 35 presenting the PSDs, refer to the validation in the frequency domain, while Table 13 shows summary of statistical data similar to those commented for the irregular operational waves reported in section 7.4.

The results reported in Table 13 are obtained by comparing the experimental and numerical time histories of the device motions. An example of time histories related to pitch motion is reported in Fig. 36. The time history related to the surge motion and the load at the fairlead of bow mooring line 4 are reported in Fig. 37. It is worthful noticing how the peak of the surge motion corresponds to the peak of the mooring line tension at least for the experimental acquisitions. In the numerical model the same behaviour can be observed for the maximum value of the fairlead tension at different time instants.

To validate statistically the prediction of the loads for the mooring lines dimensioning, the environmental contours relating to the installation site and the combination of wave height and periods for the extremes have been identified. Each wave has been repeated with ten different seeds and for each simulation, through the POT procedure detailed for operative waves, a GEV distribution has been created considering the 95th percentile. From the obtained distribution, the Most Probable Maxima (MPM) has been selected for the load dimensioning. If the numerical model predicts well the experimental data fit, the dimensioning load of the mooring lines is also accurately predicted. Fig. 38 adds practical validation to a strong statistical basis during the design of the mooring lines. In fact, this methodology, compliant with all current regulations, can be considered a key procedure when dimensioning a mooring system for wave energy converters of this type.

8. Conclusions

In this paper, the validation of numerical models against experimental tests was carried out. It was seen that under operating conditions, where linearity assumptions are more likely to be true, the numerical model effectively estimates wave-frequency device motions such as heave and pitch. For the surge motion, characterized by low frequencies, the numerical model is less accurate. This may be due to two causes: the first is the experimental uncertainty about the static position of the device at the beginning of the tests, and the second is the estimation of drag coefficients related to the hull, chains, and jumpers. After generating a wave train, the device settles into a static equilibrium position different from its initial position, thus changing the mooring stiffness. Due to the weight of the chains and the position of the device, it was not possible to reconfigure the device into its original position, but this was done only at the end of the day when the hull was taken out of the water. In the Orcaflex© environment, on the other hand, the test always began with the hull in its initial static position. In addition, in the numerical model, the drag coefficients of the chains and the jumper were associated with their nominal dimensions, the diameter for the chains, and the radius for the jumper and calculated through the conventional treatment and thus considered constant and not scaled with the Reynolds number. The surge viscous damping was not included in the numerical model therefore the accuracy of the numerical model reliability for surge motion is limited.

In any case, low-frequency surge motion is more difficult to model than others, and in future studies, the higher-fidelity CFD models will be used to determine viscous parameters to include in the PEWEC linear numerical model. The presented validation focuses on the frequency response of the complete system; thus, it can be referred to any sea state with a spectrum defined in the frequency range identified during the experiments. This peculiarity allows to apply the design methodology to other installation sites by simply changing the environmental conditions of the numerical models: i.e., generating different operational and extreme waves and adjusting the mooring system on the installation site depth. One of the main objectives of the experiments was to validate mooring stresses in extreme events. It was shown, in accordance with the methodologies proposed by DNV (Det Norske Veritas, 2014), that the numerical models predict well the design load even if some low-frequency effects are neglected, and thus can be used to certify the mooring system for future evaluations. Once the linear numerical model has been validated, the great advantage is to be able to perform optimization analysis and all simulations necessary at a low computational

Table 13
Root Mean Square Deviation, Standard Deviation error and Correlation Coefficient for surge heave and pitch motion: experimental VS numerical.

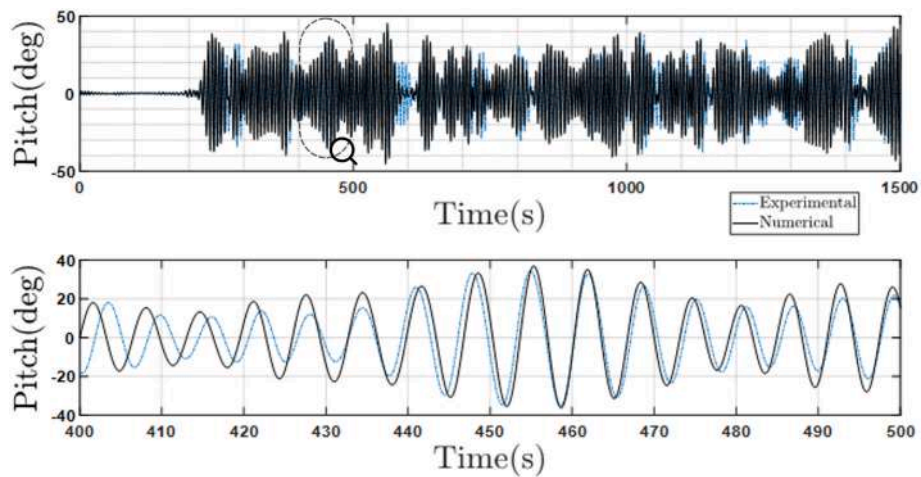| DOF	Surge			Heave			Pitch		
	RMSD	STD$_{Err}$ (%)	CC	RMSD	STD$_{Err}$ (%)	CC	RMSD	STD$_{Err}$ (%)	CC
IRR$_{EX\_seed1}$	4.7	2.4	0.62	0.71	4.9	0.75	5.2	10.2	0.8
IRR$_{EX\_seed2}$	4.2	1.4	0.63	0.74	0.21	0.76	7.1	9.1	0.82
IRR$_{EX\_seed3}$	4.5	1.8	0.63	0.72	2.1	0.77	6.1	9.5	0.85

Fig. 36. Pitch time history of extreme irregular wave Ex. Irr. 01: on top 1500s of time history, on bottom a zoom of 100s.
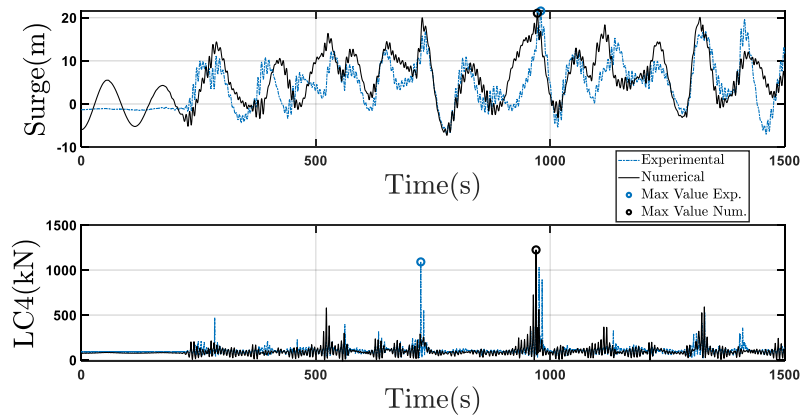

Fig. 37. Time histories of surge and load at fairlead of mooring line 4.
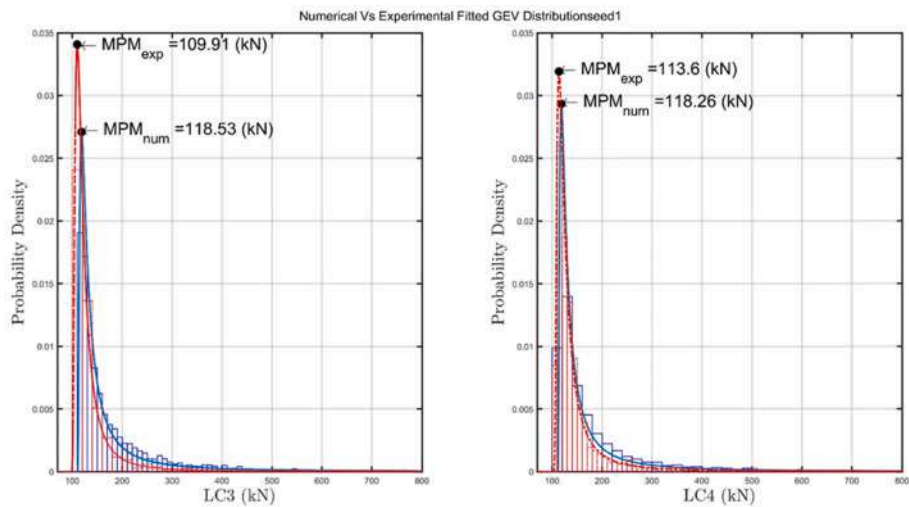

Fig. 38. GEV distribution obtained through POT procedure for experimental and numerical data.

cost. For the development of the PEWEC technology, the validation of the mooring system tested in an operative environment is crucial for TRL improvement.

CRediT authorship contribution statement

F. Niosi: Conceptualization, Methodology, Study design, Software, Validation, Formal analysis, Investigation, Resources, Data curation,

Writing – original draft, Writing – review & editing, Visualization. **E. Begovic:** Conceptualization, Formal analysis, Resources, Writing – original draft, Writing – review & editing, Supervision. **C. Bertorello:** Resources, Supervision, Project administration. **B. Rinauro:** Formal analysis, Investigation, Resources, Writing – original draft, Writing – review & editing. **G. Sannino:** Project administration, Funding acquisition. **M. Bonfanti:** Conceptualization, Methodology, Study design, Investigation, Data curation, Supervision, Project administration. **S.A. Sirigu:** Conceptualization, Methodology, Study design, Investigation, Data curation, Supervision, Project administration.

Declaration of competing interest

The authors declare that they have no known competing financial interests or personal relationships that could have appeared to influence the work reported in this paper.

Data availability

The data that has been used is confidential.

References

Barltrop, N.P.D., 1998. Floating Structures: A Guide for Design and Analysis. Oilfield Pubns Inc.

Barrera, C., Guanche, R., Losada, I., 2019. Experimental modelling of mooring systems for floating marine energy concepts. Mar. Struct. 63, 153–180. https://doi.org/10.1016/j.marstruc.2018.08.003.

Bonfanti, M., Giorgi, G., 2022. Improving computational efficiency in WEC design: spectral-domain modelling in techno-economic optimization. J. Mar. Sci. Eng. 10 (10), 1468. https://doi.org/10.3390/jmse10101468.

Bonfanti, M., Sirigu, S.A., 2023. Spectral-domain modelling of a non-linear wave energy converter: analytical derivation and computational experiments. Mech. Syst. Signal Process. 198, 110398 https://doi.org/10.1016/j.ymssp.2023.110398. ISSN 0888 3270.

Cerveira, F., Fonseca, N., Pascoal, R., 2013. Mooring system influence on the efficiency of wave energy converters. Int. J. Mar. Energy 3–4. https://doi.org/10.1016/j.ijome.2013.11.006.

Clemente, D., Rosa-Santos, P., Taveira-Pinto, F., 2021. On the potential synergies and applications of wave energy converters: a review. Renew. Sustain. Energy Rev. 135.

Cummins, W.E., 1962. The impulse response function and ship motions. Schiffstechnik 9, Heft 47, 101–109.

Det Norske Veritas (DNV), 2014. DNV-RP-C205 Environmental Conditions and Environmental Loads, pp. 1–182. Dnv, no. April.

Elhanafi, A., Macfarlane, G., Fleming, A., Leong, Z., 2017. Experimental and numerical investigations on the intact and damage survivability of a floating–moored oscillating water column device. Appl. Ocean Res. 68, 276–292. https://doi.org/10.1016/j.apor.2017.09.007.

Fontana, M., Casalone, P., Sirigu, S.A., Giorgi, G., Bracco, G., Mattiazzo, G., 2020. Viscous damping identification for a wave energy converter using CFD-URANS simulations. J. Mar. Sci. Eng. 8, 5. https://doi.org/10.3390/JMSE8050355.15.

Fenu, B., Attanasio, V., Casalone, P., Novo, R., Cervelli, G., Bonfanti, M., Sirigu, S.A., Bracco, G., Mattiazzo, G., 2020. Analysis of a Gyroscopic-Stabilized Floating Offshore Hybrid Wind-Wave Platform. J. Mar. Sci. Eng. 8, 439. https://doi.org/10.3390/jmse8060439.

Fenu, B., Niosi, F., Paduano, B., Sirigu, S.A., 2022. Experimental investigation of 1:25 scaled model of Pendulum Wave Energy Converter. In: 2022 International Conference on Electrical, Computer, Communications and Mechatronics Engineering (ICECCME), Maldives, Maldives, pp. 1–6. https://doi.org/10.1109/ICECCME55909.2022.9987910.

Golbaza, D., Asadib, R., Aminic, E., Mehdipourb, H., Nasirid, M., Etaatie, B., Naeenib, S.T.O., Neshatf, M., Mirjalilif, S., Gandomi, A., 2022. Layout and design optimization of ocean wave energy converters: a scoping review of state-of-the-art canonical, hybrid, cooperative, and combinatorial optimization methods. Energy Rep. 8, 15446–15479. https://doi.org/10.1016/j.egyr.2022.10.403.

Gubesch, E., Abdussamie, N., Penesis, I., Chin, C., 2022. Effects of mooring configurations on the hydrodynamic performance of a floating offshore oscillating water column wave energy converter. Renew. Sustain. Energy Rev. 166.

Johanning, L., Smith, G.H., Wolfram, J., 2006. Mooring design approach for wave energy converters. Proc. IME M J. Eng. Marit. Environ. 220, 159–174. https://doi.org/10.1243/14750902JEME54.

Khalid, F., Arini, N., Johanning, L., 2019. D2.4 Recommendations for WEC Mooring Guidelines and Standards Title Recommendations for WEC Mooring Guidelines and Standards Change Record Revision Date Description Reviewer EXECUTIVE SUMMARY".

Mancini, S., Begovic, E., Day, A.H., Incecik, A., 2018. Verification and validation of numerical modelling of DTMB 5415 roll decay. Ocean Eng. 162, 209–223. https://doi.org/10.1016/j.oceaneng.2018.05.031.

Morison, J.R., O'Brien, M.P., Johnson, J.W., Schaaf, S.A., 1950. The forces exerted by surface waves on piles. In: Petroleum Trans., AIME, 189, pp. 149–157.

Newman, J.N., 2017. Marine Hydrodynamics, 40th anniversary edition. The MIT Press, Cambridge, MA.

Niosi, F., Battisti, B., Sirigu, S.A., 2022. Influence of hydrodynamic interactions on the productivity of PEWEC wave energy converter array. In: International Conference on Electrical, Computer, Communications and Mechatronics Engineering. ICECCME, Maldives, Maldives, pp. 1–6. https://doi.org/10.1109/ICECCME55909.2022.9988093.

Niosi, F., Parrinello, L., Paduano, B., Pasta, E., Carapellese, F., Bracco, G., 2021. On the influence of mooring in wave energy converters productivity: the PEWEC case. In: International Conference on Electrical, Computer, Communications and Mechatronics Engineering. ICECCME, Mauritius, Mauritius, pp. 1–6. https://doi.org/10.1109/ICECCME52200.2021.9590867.

Orcina, 2020, 10.1b Edition. OrcaFlex-Documentation.

Ogilvie, T.F., 1964. Recent Progress toward the Understanding and Prediction of Ship Motions, ACR-112, pp. 3–79.

Paduano, B., Giorgi, G., Gomes, R., Pasta, E., Henriques, J., Gato, L., Mattiazzo, G., 2020. Experimental validation and comparison of numerical models for the mooring system of a floating wave energy converter. J. Mar. Sci. Eng. 8 https://doi.org/10.3390/jmse8080565, pg 565.

Pozzi, N., Bracco, G., Passione, B., Sirigu, S.A., Vissio, G., Mattiazzo, G., Sannino, G., 2017a. Wave tank testing of a pendulum wave energy converter 1:12 scale model. Int. J. Appl. Mech. 9, 2. https://doi.org/10.1142/S1758825117500247.

Pozzi, N., Bracco, G., Passione, B., Sirigu, S.A., Mattiazzo, G., 2017b. PEWEC: experimental validation of wave to PTO numerical model. Ocean Eng. 167, 114–129. https://doi.org/10.1016/j.oceaneng.2018.08.028, 2018.

Pozzi, N., Bonetto, A.M., Bonfanti, M., Bracco, G., Dafnakis, P., Giorcelli, E., Passione, B., Sirigu, S.A., Mattiazzo, G., 2018a. PeWEC: Preliminary Design of a Full-Scale Plant for the Mediterranean Sea.

Pozzi, N., Bonfanti, M., Mattiazzo, G., 2018b. Mathematical modeling and scaling of the friction losses of a mechanical gyroscope. Int. J. Appl. Mech. 10 https://doi.org/10.1142/S1758825118500242.

Qiao, D., Haider, R., Yan, J., Ning, D., Li, B., 2020. Review of Wave Energy Converter and Design of Mooring System. Sustainability 12. https://doi.org/10.3390/su12198251.

Sirigu, S.A., Bonfanti, M., Passione, B., Ermina, B., Carlo, B., Dafnakis, P., Bracco, G., Giorcelli, E., Mattiazzo, G., 2018. Experimental Investigation of the Hydrodynamic Performance of the ISWEC 1:20 Scaled Device.

Sirigu, S.A., Foglietta, L., Giorgi, G., Bonfanti, M., Cervelli, G., Bracco, G., Mattiazzo, G., 2020. Techno-economic optimisation for a wave energy converter via genetic algorithm. J. Mar. Sci. Eng. 8, 482. https://doi.org/10.3390/jmse8070482.

Windt, C., Faedo, N., García-Violini, D., Peña-Sanchez, Y., Davidson, J., Ferri, F., Ringwood, J.V., 2020. Validation of a CFD-Based Numerical Wave Tank Model of the 1/20th Scale Wavestar Wave Energy Converter. Fluids 2020 (5), 112. https://doi.org/10.3390/fluids5030112.

Wright, C.S., Yoshimoto, H., Wada, R., Takagi, K., 2022. Surge slow drift viscous drag damping of an advanced spar: A numerical–experimental method for variable damping rates. Ocean Eng. 266 (2), 112696, ISSN 0029-8018. https://doi.org/10.1016/j.oceaneng.2022.112696.

Xu, S., Wang, S., 2019. Review of mooring design for floating wave energy converters. Renew. Sustain. Energy Rev. 111, 595–621. https://doi.org/10.1016/j.rser.2019.05.027.